ICE-CAMERA: a flatbed scanner to study inland Antarctic polar precipitation.

Massimo Del Guasta

Istituto Nazionale Ottica CNR, Sesto Fiorentino, 50019, Firenze, Italy

Correspondence to: Massimo Del Guasta (massimo.delguasta@ino.cnr.it)

Abstract.

Studying precipitation at very high latitudes is difficult because of the harsh environmental conditions that limit the external activity of humans and instruments, especially in the polar winter. The direct monitoring of ice crystal habits and size distribution in antarctic precipitation is important for the validation of the algorithms used for retrieving precipitation from ground-based and satellite-borne radar instruments, and for the improvement of the climatological modeling of polar areas. The paper describes an automated device (ICE-CAMERA) specifically developed for the imaging, measurement and classification of ice precipitation on the Antarctic high plateau. The instrument gives detailed information on precipitation on an hourly basis. The article provides a description of the device and its image processing software. Starting in 2014, the instrument operates *almost* unattended all year round at Concordia station, Antarctica (75°S, 123°E, 3220 m altitude).

1. Introduction.

In Antarctica, the characteristics of ice precipitation depend greatly on the region. In coastal areas, precipitation is influenced by synoptic scale features, such as cyclones and fronts (Bromwich, 1988). In the interior (> 2500 m), a significant part of the precipitation falls in the form of small ice crystals ("diamond dust", DD) under clear-sky conditions (Fujita and Abe, 2006). Snow particles over Antarctica are generally smaller compared to other regions of the world. The largest particles are found close to the coast, where more water vapour is available and diameters up to 10 mm are recorded (Konishi et al., 1992) with particle shapes similar to mid-latitude ones (Satow, 1983). More inland stations record snowflakes of much smaller sizes, ranging from particles smaller than 100 μm at South Pole (Walden et al., 2003, Lawson et al., 2006) till hundreds of μm at other inland stations (Lachlan-Cope et al., 2001).

In situ measurements of precipitation are rare in Antarctica and affected by large uncertainties. This is particularly true in the high plateau, where less than 20 cm of snow accumulates every year (Palerme et al.,2014). As a result, the global precipitation products that rely on these observations (i.e. the Global Precipitation Climatology Centre (GPCC), (Schneider et al., 2017)) have no coverage over this region. Other observational products, such as the Global Precipitation Climatology Project (GPCP) (Huffman et al.,2001) , that uses GPCC for bias correction over land, has relied on satellite-only precipitation estimates. Satellite products also face large uncertainties over cold regions such as Antarctica due to insufficient sensitivity of sensors to detect and estimate precipitation signals, complex surface emissivities, and poor understanding of precipitation microphysics. Ground based K-band radars (~1-cm wavelength) are robust instruments successfully employed for studying precipitation in coastal Antarctic sites (Souverijns et al., 2017) but are quite blind to the sub-millimetre ice particles encountered on the plateau, due to the relationship D^6 between the radar scattering cross-section and the particle diameter (D).

The satellite-borne radar CloudSat (Liu, 2008) did provide a quantum leap in observing ice in the Antarctic atmosphere (up to 82 °S), but being a single-frequency radar (like K-band radars), the retrieval of precipitation quantities relies on many assumptions about the properties of particles, resulting into ±50% uncertainties for IWC (Heymsfield et al.,2008). The microphysical assumptions (shapes and size distribution of particles) are the biggest causes for IWC, IWP, and snowfall rate retrieval uncertainty (Hiley et al.,2011, Wood et al.,2015). Moreover, CloudSat bins close to the ground cannot be used for precipitation retrieval, resulting into a severe underestimation of the diamond-dust and blowing-snow contribution to Antarctic snow balance (Palm et al., 2018). Despite these uncertainties, in absence of ground validation CloudSat data are now used as independent data set for the validation of precipitation models in Antarctica (Palerme et al.,2014, Palerme et al.,2017).

43 The direct observation and the continuous monitoring of habit and size distribution of precipitation is therefore required in

44 order to validate both precipitation models, CloudSat and radar algorithms on the Antarctic plateau.

45 Disdrometers are robust *in-situ* devices, increasingly used in Antarctic coastal areas (Bracci et al.,2022). They provide the size

46 distribution and falling speed of hydrometers, but they give no direct information about the shape. The evolution of

47 disdrometers into 2D-disdrometers gave access to some shape indications about hydrometeors (Grazioli et al.,2014). A further

48 evolution of disdrometers into Imaging-disdrometers, such as the Snowflake Video Imager (SVI) (Newman et al., 2009),

49 provided realistic images of the crystals. Grazioli et al., (2017), as part of a multidisciplinary field campaigns, deployed a

50 multi-angle snowflake camera (MASC) to take photographs of individual snow particles. This instrument, representing a

51 further advance in the field of imaging disdrometers, collects high-resolution stereoscopic photographs of snowflakes in free

52 fall while they cross the sampling area (Garrett et al., 2012), thus providing information about snowfall microphysics (Praz et

53 al., 2017). The optical structure of the imaging-disdrometer and the MASC makes these instruments reliable in the presence

54 of millimetre-sized hydrometeor precipitation. In Antarctica, their practical application is mainly limited to coastal areas.

55 The direct observation of inner Antarctic particles requires imaging techniques with resolution of a few microns. Photographic

56 studies of precipitation in the interior of the Antarctic are quite rare, carried out primarily at the South Pole Station (SPS)

57 through formvar replicas. In early works with formvar, Hogan (1975) identified at SPS millimetre-sized columnar crystals and

58 column- and bullet-rosettes in cloud precipitation, and smaller ($\cong$100 μm diameter) platelike particles in clear-sky

59 precipitation. Satow (1983), working with formvar replicas on Mizuho plateau found prevalently single bullets and

60 combination of bullets. Long solid column crystals were also found (with an air temperature range from -42°C to -56°C) with

61 a mean length of 290 μm and a maximum length of 1.2 mm, with a mean aspect ratio of 18. Small (50-400 μm) hexagonal,

62 triangular, scalene and square plates were also observed. Kikuchi and Hogan (1979) collected formvar replicas of DD in the

63 summer at SPS, finding columnar crystals of 90 μm average lengths and plates as small as 50 μm in diameter. Ohtake and

64 Yogi (1979) classified winter ice crystal precipitation in Antarctica under six categories. These included large rosettes, bullets

65 and columns (millimetre-sized), thin hexagonal plates and columns (200 μm or less), and smaller crystals of various shapes

66 including triangular and polyhedral. Shimizu (1963) observed "long column" crystals in the winter at Byrd Station (80S,

67 120W). Size distributions of Antarctic DD in winter and spring were reported by Smiley et al. (1980) for particles larger than

68 50 um: they observed the same ice crystal forms that were reported earlier. Walden et al. (2003) studied DD, blowing snow,

69 and cloud precipitation in winter, at SPS, by collecting crystals on slides and analyzing them using microphotography. In their

70 study, columns with an average length of 60 μm and plates with an average diameter of 30 μm were found in DD. The direct

71 observation of ice precipitation on the plateau was typically carried out by means of formvar replicas and/or microphotography,

72 but these techniques take time, are difficult to implement throughout the year and are necessarily limited to short field

73 campaigns and samples of very limited size. Designing automatic instruments for the continuous, photographic study of

74 precipitation in such a harsh environment necessarily require several compromises between the high resolution of

75 microphotography and the robustness of outdoor optical instruments such as disdrometers. Lawson et al. (2006) worked at

76 SPS, in summer, using innovative Cloud Particle Imagers (CPIs), which replaced formvar replicas. This technique allowed the

77 automatic analysis of around 700,000 DD crystal images in terms of caliper size, aspect ratio and other shape parameters. An

78 automatic classification software, based on shape parameters, was used to categorize the images into nine simplified classes:

79 small plates and spheroids, columns, thick plates, plates, budding rosettes, rosettes, complex with side planes, irregulars.

80 Concordia International Station, located on the Dome-C (DC, 75°S,123°E, 3220 m above sea level) is a special location to test

81 new instruments for precipitation studies. Surface temperatures seldom exceed -25°C in summer, whereas winter temperatures

82 can reach -85°C. The 3 m average wind speed is 3 ms^{-1} for Aristidi (2005) and 4.5

83 ms^{-1} (hourly-averaged) for Argentini et al. (2014). The strongest winds (up to 15 ms^{-1}, hourly-averaged) blow from the

84 continental regions. These winds are due to gravity flows from the inner plateau regions south of Dome C, and are more often

85 observed during the winter, especially in coincidence with warming events. The circulation at the surface during the summer

86 is affected, especially in daytime, by the synoptic circulation. In summer the wind speed oscillates during the day, with values
87 increasing (by a few ms^{-1}) in the afternoon, when a convective layer develops, leading to the increase of the wind speed
88 (Argentini et al.,2014). Relative humidity relative to ice is typically around 55-85% (Genthon et al., 2022). In these conditions,
89 precipitation of ice crystals can be studied by simply collecting them on horizontal surfaces. This is done at DC by hand,
90 starting in 2008, collecting precipitation on flat surfaces ("benches") and visually inspecting it. This analysis is restricted to
91 one observation per day, a rate that is difficult to increase, especially in winter. The analysis of these samples is also time-
92 consuming and often subject to biases due to ice re-processing and sublimation, hoar formation, and subjective judgement of
93 the shape and relative abundance of ice particles. Schlosser et. al (2017) relied on this manual observation and classification
94 of ice particles in his analysis of precipitation isotope data at DC. They classified the ice grains into diamond dust, drifting
95 snow, snow and frost (hoar). The prevalence of hoar in the observed daily precipitation record (with temperatures below -
96 50°C) indicates the limitations of this manual technique if detailed information on DC precipitation particles is desired.
97   Detailed work was carried out in DC on a few individual DD and cloud precipitation crystal replicas by means of SEM electron
98 microscopy by Santachiara et al. (2016). They also analyzed very small particles (10-50 μm), in a size range inaccessible to
99 ordinary   optical   methods.
100 The purpose of developing ICE-CAMERA was to fill a gap in precipitation monitoring at Concordia with a robust instrument
101 capable of monitoring with continuity, all-year round, habit and size of ice particles in precipitation, while avoiding some of
102 the problems associated with the visual inspection of precipitation. This was achieved through the combined development of
103 robust camera equipment and machine learning techniques for sizing and classifying ice crystals.

2.1 Overview of the instrument.

ICE-CAMERA is a flatbed scanner (Zheleznyak et al, 2015), whose operating principle is the same as that of ordinary
flatbed scanners in offices. In the case of ICE-CAMERA, it specially designed for observing polar precipitation in the harsh
environmental conditions of Concordia station (Fig. 1). Within this work, the term "precipitation" will include both
"diamond dust" and cloud precipitation.
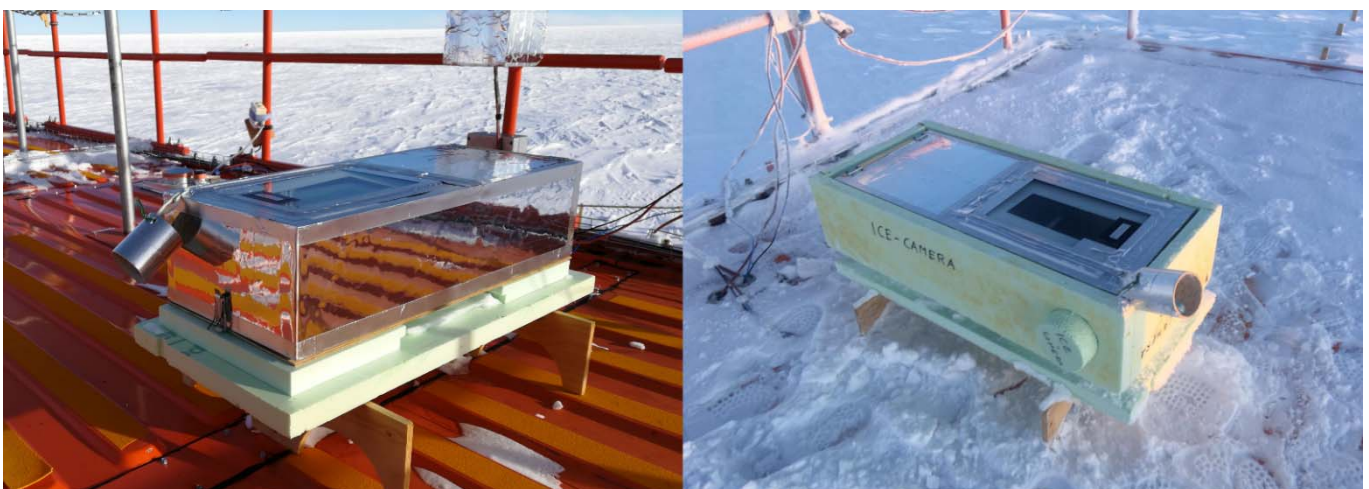
Fig. 1: ICE-CAMERA with its summer sun-shield (left) and with the winter coat (right).

119   The principle is simple: at the low temperatures and low wind speeds encountered at DC, precipitation falling on a horizontal

120   glass surface accumulates with time until it sublimates, leaving plenty of time for scanning the glass surface for counting and

121   measuring individual ice particles. The scanning, like in ordinary flatbed scanners, is performed by means of a line-scan camera

122   (Sect.2.2). moved by a motorized scan sledge, and looking up at the DS through a 45° mirror (Fig. 2). The focus of the camera

123   is adjusted by a small motorized focusing sledge moving the 45° mirror (Sect.2.3). During the scan, the image is sent to the

124   PC,   located   inside   the   shelter.

125   After a complete scan of the DS, the glass is heated and the precipitation sublimated (section 2.7). Once cooled down, the

126   clean SD begins to accumulate new particles. This cycle takes place every hour. After each image acquisition, the MATLAB

127   image processing code is called to process the DS image, and a summary-image containing only segmented particles (if

128   present) is stored for post-processing. (Sect. 4.1.3). Every particle is also automatically measured through image processing

129   (Sect. 4.1) and classified through machine learning (Sect.4.2). Individual particle data are stored in rows in a text file, along

130   with weather and housekeeping data, for post-processing and statistical analysis.

131
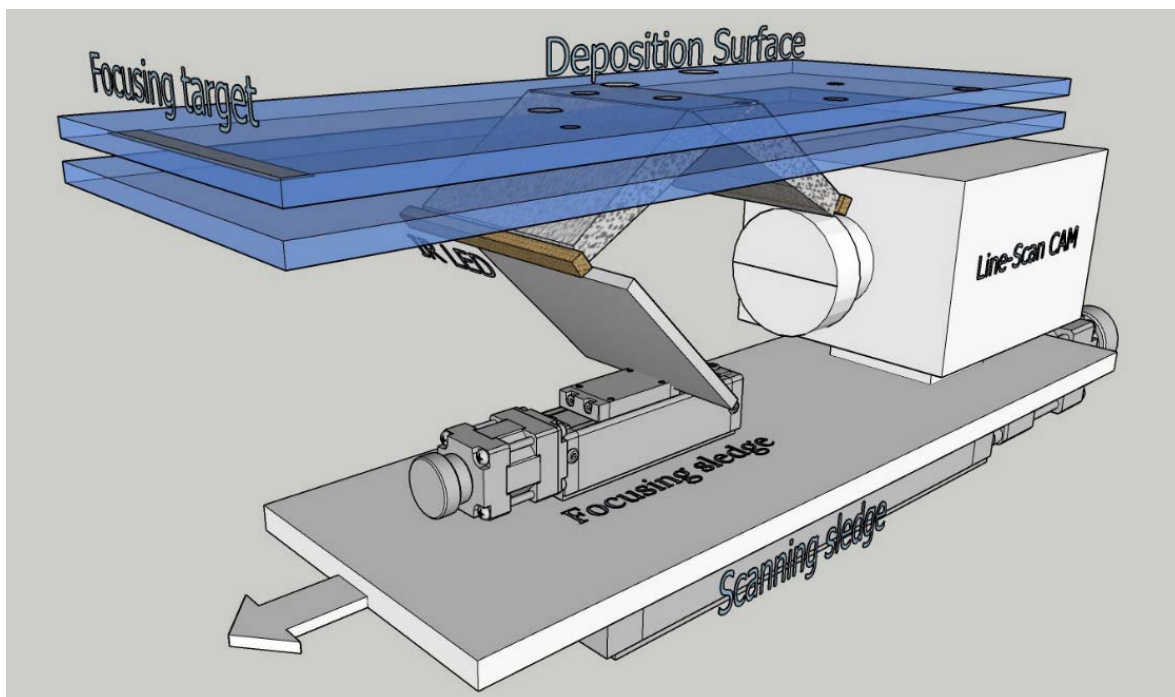
132

133   **Fig. 2: ICE-CAMERA basics: the scan sledge moves the image-acquisition line along the deposition surface. The focusing sledge**

134   **adjusts the focus.**

135

136   All basic operations of ICE-CAMERA, (with the exception of CAM acquisition) are driven by a custom microprocessor

137   (Microchip PIC) logic board (Fig. 3). The same PIC board reads the housekeeping temperature sensors (attached to the DS

138   and placed inside and outside the instrument), drives the stepper motors of the sledges as well as pumps and fans. The PIC

139   Board communicates with the main computer (located inside the shelter) through RS232. NI Labview software controls image

140   acquisition, reads maintenance data, and monitors PIC operations along the RS232 line. The line-scan camera communicates

141   with the PC via Gigabit Ethernet.

142   The instrument is placed outdoor, on the roof of the "Physique" shelter, approximately 6 m above the ground.

143   ICE-CAMERA was first installed in Concordia in 2012, but replaced in 2014 with its improved version, described here.

144   From then on, the instrument works year-round to produce precipitation data, every hour. Standard meteorological data are

145   automatically obtained from local weather station AWS MILOS 520.

146

147
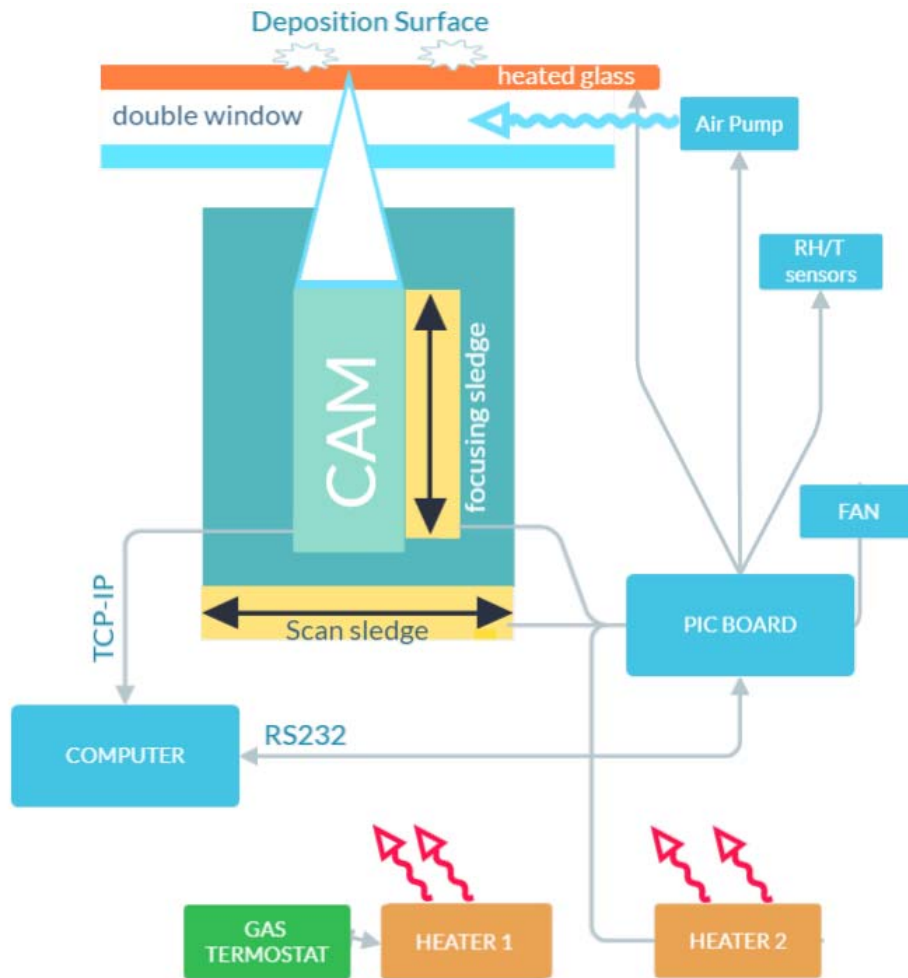
148
149
150 **Fig. 3: Basic schematics of the instrument**

151
152
153
154 **2.2 The line scan Camera.**

155 A linear scanning GigE Vision monochrome camera (Schafter-Kirchoff SK7500VTF-XB (52.5 mm sensor, 7500 pixels,
156 7x7μm pixels, 8.2kHz line frequency), equipped with a 1:1 macro lens (APO-Rodagon D1X, f5.6) is used for the acquisition.
157 The optics were designed by Schafter-Kirchoff in order to have a resolution equivalent to the 7μm pixel size. A 90° bending
158 aluminium mirror is used to look upward. The illumination is ensured by 850 nm LEDs. A colour filter (Schott RG715, 800-
159 1000 nm band-pass) was used on the CAM lens, in order to have a fully solar instrument. The line-scan camera assembly is
160 moved by a motorized sledge at a speed of 8 mm s^{-1} in order to scan a rectangular surface of 55x200 mm, (Deposition Surface,
161 DS), at the center of the window. The final image is 7500*30000 pixel, 12 bits, monochrome. A fine calibration of the actual
162 pixel size of the DS image was achieved by scanning a calibrated grid (0.1mm spacing) placed on the DS.

163

2.3 The Focusing.

In working conditions, the focal depth is ±0.5 mm. A preliminary and accurate alignment of the motorized sledge plane to the DS ensures uniformity of focus across the DS at room temperature. A motorized focusing sledge, moving the bending mirror, allows to adjust the focus in operating conditions (Fig. 2). As ICE-CAMERA works outdoor at DC, it can experience a broad internal temperature range, from +5°C in summer to -45°C in winter, with quite large temperature gradients across the structure. Thermal expansion and changes in optical refractive indexes result in unpredictable changes in the focal plane. The correction of the focus is thus automatically performed, every 6 hours, by bringing the measuring sledge outside the DS, where a focusing spot (a sandpaper strip) is glued to the window (Fig. 4).
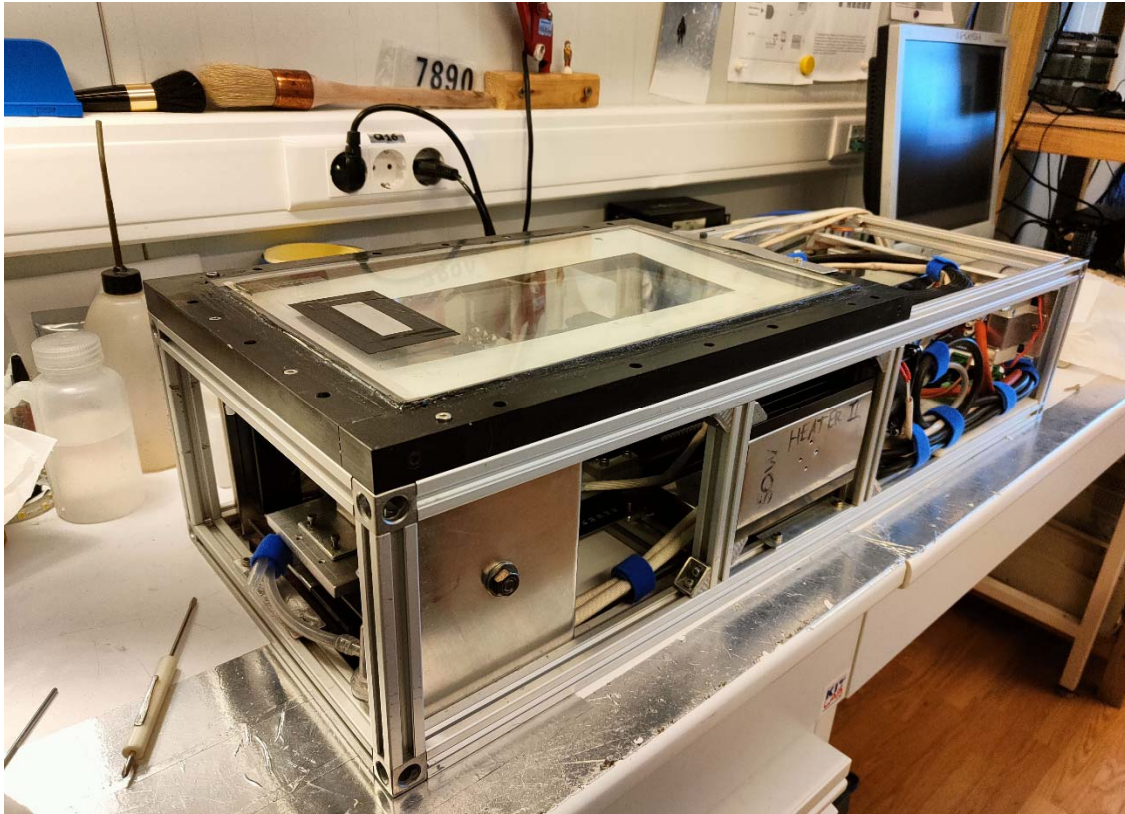
Fig. 4: ICE-CAMERA out-of-the-box. The focus target if fixed onto the DS window

The porous structure of the sandpaper has a length-scale of the order of 0.1 mm, comparable with the size of the measured ice particles. While calibrating, the focusing sledge is moved by ±2 mm around the actual position in 0.25 mm steps. Successive images of the sandpaper are taken and their contrast (defined as the standard deviation of the intensity of the pixels) is measured. After a Gaussian-fit of the contrast as a function of defocusing (Fig. 5), the position corresponding to the maximum contrast is obtained, and the mirror sledge is moved into that position. The typical focal spot adjustment between two consecutive calibrations if 0-0.25 mm. The calibration takes approximately 5 minutes. For this reason, it is not done after each measurement, so as to save PC resources for data processing.
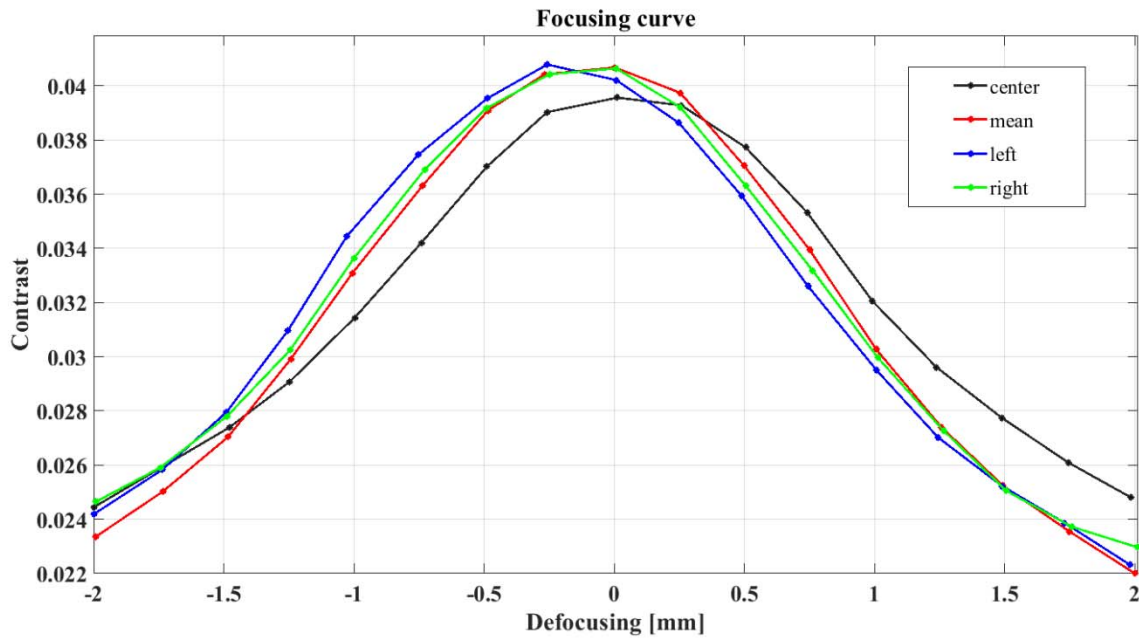
Fig. 5: Typical focus calibration: Contrast is calculated in three sectors of the image: center, left and right. The contrast throughout the image is also displayed (red). The slight difference in focus (0.2mm) between the center of the image and the side wings is a normal lens effect.

2.4 Illumination.

Lighting is supplied by two 850 nm LED (TSHG6200) strips. Both arrays illuminate the scan line symmetrically and approximately 45° from the optic axis in order to minimize multiple reflections in the double window and within the camera lens. Infrared illumination was chosen in order to work in solar-blind conditions. This is particularly important, as the linear scanning camera always looks upward, to the sky. The uniformity of lighting along the linear CCD image was tested by taking an image of the same sandpaper used in the focus. The intensity profile along the CCD image was measured, and the intensity of the LEDs eventually changed to have a final intensity uniformity across the entire frame of less than 15%.

2.5 The Deposition Surface (DS).

The DS is a 10 mm thick, electrically-heated glass (E-GLAS, Saint-Gobain). This glass is transparent at 850 nm, and is electrically heated with 45 V ac, 1000 Wm^{-2} when sublimating the ice particles. A second, 2 mm thick, optically graded glass sheet (an ordinary flatbed scanner optical glass), placed 13 mm under the DS, makes up with the DS a double window. This arrangement is necessary in order to keep the DS thermally insulated from the heated, interior of the instrument. A thermocouple is attached to the DS, while other thermocouples monitor window inter-space temperatures. A DS temperature of (at least) 3 °C above air temperature is enough to prevent the formation of frost on it in any season, as suggested by Tremblin et al., (2011) (Fig. 6).

206

Fig. 6: ICECAMERA at -70°C, Concordia station winter: the DS if free of frost

207
208
209
210

211 During the sublimation period (Sect.2.7), ambient air is pumped for five minutes by means of a 3.5 l/m miniature pump

212 through the double window space, in order to keep the internal surfaces of the double window always free of frost . Using

213 inert gases such as argon in the double window space for the same purpose proved unsuccessful in Concordia at the

214 extremely low winter temperatures. In order to avoid the eventual accumulation of wind-drifted snow, the DS has no walls or

215 obstacles all around. Furthermore, the instrument is located on the roof of a shelter, almost 6 meters above the ground, an

216 altitude where blowing snow is not normally important at Concordia. Libois et al. (2014) identify drifting snow events at

217 Dome C when the 10-m wind speed exceeds 7 m s^{-1}. Assuming a logarithmic wind speed profile between the surface and

218 10-m and an aerodynamic roughness length value of 1 mm (Vignon et al., 2016), this corresponds to a wind speed threshold

219 value of 5 m s^{-1} at 6 m above the ground. Winds below this threshold (near the annual average wind speed in DC) are not

220 expected to carry blowing snow to the DS. In addition, blowing snow impacts the flat horizontal and smooth DS at very

221 small angles, with a very limited chance of sticking to it. As a consequence, ice particles collected on the SD can be

222 considered representative of precipitation. Since DS is warmer than air, there is no secondary growth in deposited ice.

223 Instead, the partial sublimation of ice particles before scanning could not be excluded, especially in summer. This topic

224 needs additional field work and will be modelled in Sect. 3.2.

225

226 **2.6 The thermal control.**

227 The temperatures measured by the ICE-CAMERA sensors are continuously transferred to the computer. The NI-Labview

228 software controls the internal temperature of ICE-CAMERA above -40°C, and the DS temperature always under -5°C ("Heater

229 2" in Fig. 3). These conditions are maintained throughout the year during every phase of the measuring cycle. An independent

230 wired thermostatic system ensures backup temperature control in the event of a PC or PIC board failure ("Heater 1" in Fig. 3).

231 After a black-out, when the power is restored, a timer is used to heat the inside of the instrument before turning on the

232 electronics. This is important at Concordia to prevent damage to standard electronics with typical operating temperatures of -

233 40°C.

234 In winter, a 40 mm thick Styrofoam coat is added around the instrument for increasing thermal insulation, whereas in summer,

235 a Mylar sunscreen prevents overheating of the DS above -5°C in the hot days (Fig. 1). In warm weather, outdoor air is carried

236 inside the box with a tangential fan, for better cooling of the instrument.
237

2.7 Sublimation-deposition cycle.

239 After an entire scan of the DS, electricity is applied to the window to sublimate the particles. The heating rate of the DS
240 depends primarily on the thermal constants of the heated window, and secondarily on the wind speed. An indoor test (Fig.
241 7), showed a heating of rate of 2.5°C min^{-1}, and a cooling rate of 1 °C min^{-1}.
242
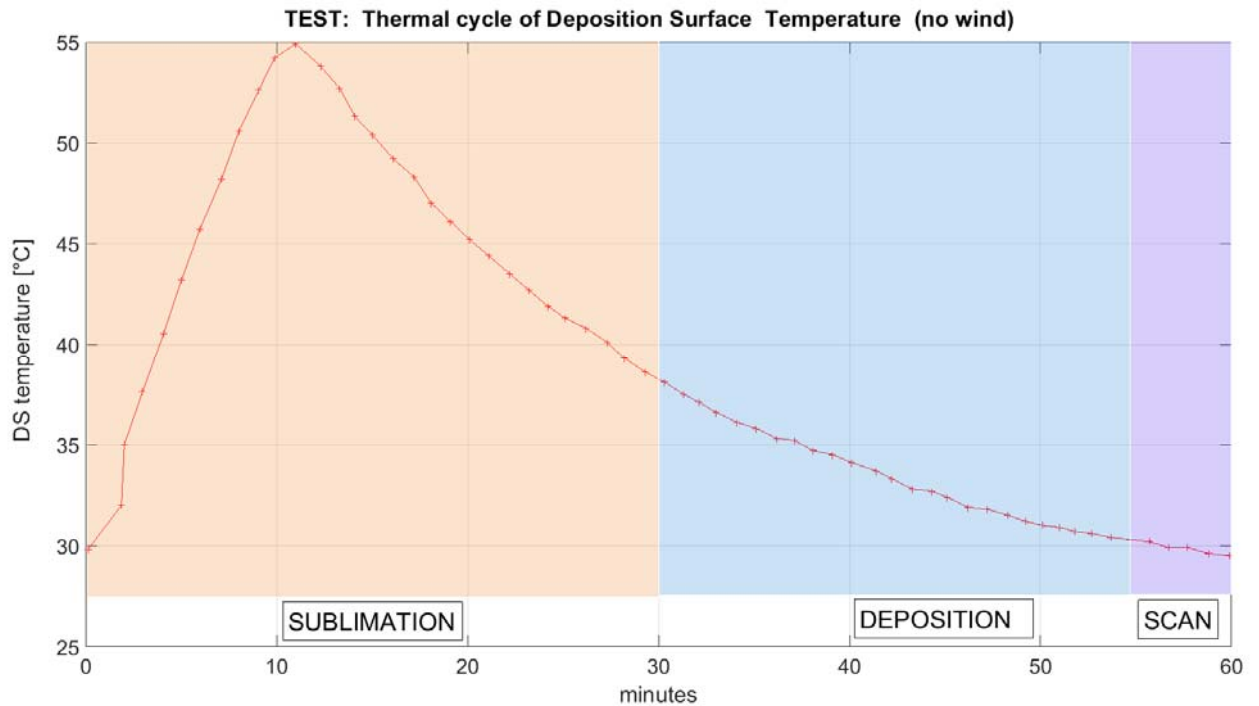
243 **Fig. 7 : Indoor test of DS heating-cooling rates within a 60 min cycle. Sublimation, Deposition and scan periods are shown**
244

245 The cooling rate is almost 50% of the heating rate just due to the sandwich-like structure of the heating-glass, with the
246 heating layer at the middle (Fig. 8).
247
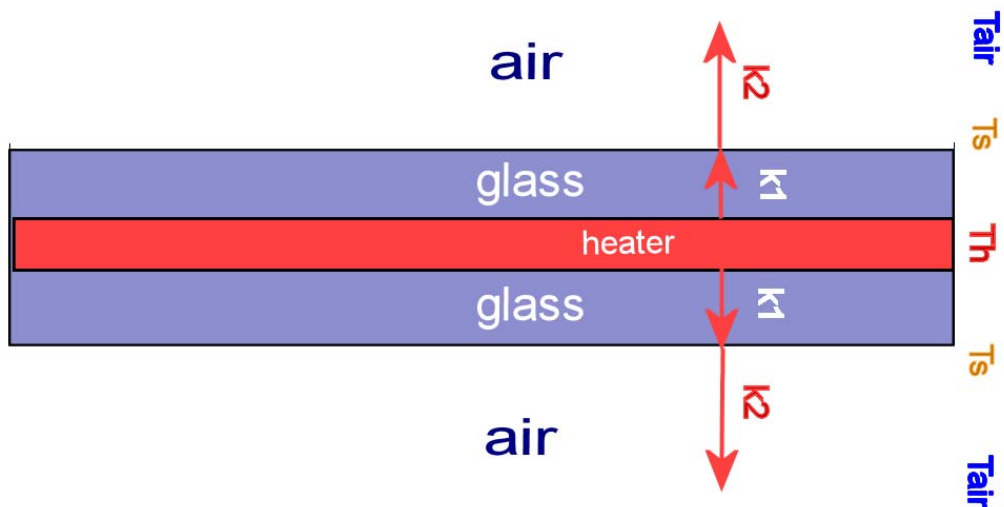
248 **Fig. 8: The thermal structure of the electrically-heated glass**
249

250 The conductive heat transfer coefficient of the glass ($k1=0.8$ W m^{-1} K^{-1}) is much greater than that of the air ($k2=0.025$ W

251 m^{-1} K^{-1}). During glass heating, heat is transferred rapidly (with thermal constant k1) to the DS from the electrically-heated

252 inner layer, while during cooling the heat transfers from the DS to the air occurs slowly (with a thermal constant closer to

253 k2).

254 Outdoor tests carried out in summer at DC (-30°C air temperature) showed a heating rate of 3 °C min^{-1} in still air, 2.5 °C

255 min^{-1} with 2.5 m s^{-1} wind speed, and 1.8 °C min^{-1} with 5 m s^{-1} wind speed. In all cases, the cooling rate was approximately

256 1.5 °C min^{-1}.

257 An outdoor sublimation test (-30°C air temperature, wind speed <3m s^{-1}) performed with snow manually spread on the DS

258 showed that, after applying heating for 10 minutes (up to a DS temperature of -8°C) the sublimation of the majority of

259 particles (diameter<1000 μm) was complete within 20 minutes after turning off the heating, with just a few big grains (initial

260 diameter>1000 μm) still present after 30 minutes.

261 After these tests, the galss heating period was set at 10 minutes (the heating is stopped anyway if the DS temperature exceeds

262 -5°C to avoid melting of the ice in summer). At the peak of the sublimation period, SD resulted warmer than air of about dT

263 = 20°C. Once the heater is turned off, and after a cooling time of 20 minutes, the DS temperature comes back warmer than

264 the air by about dT = 5°C. The "sublimation period" is considered complete, and ice particles accumulate again on the DS,

265 with no relevant sublimation ("deposition period" in Fig. 7). At the end of the deposition period, a scan of the DS is carried

266 out, for a duration of one minute. If no ice particles were detected on the previous scan, the DS heater is not applied,

267 sublimation is not needed. The effective deposition period depends on the temperature, wind and exposure to the sun in

268 summer. This uncertainty, combined with occasional wind removal and particulate sublimation (Sect. 3.2) during the

269 deposition period, prevents the use of ICE-CAMERA for rigorous quantitative precipitation studies.

270 DS surface temperature is actually measured by using a small thermocouple. This measurement implies great uncertainties due

271 to the radiant warming of the sensor in summer and the difficult thermal coupling with the glass surface. The non-contact

272 measurement of DS temperature by means of IR sensors would also be uneffective in winter conditions.

273

274 3.1 **Adhesion of ice particles on the DS.**

275 The adhesion of ice crystals to the smooth DS is caused by two principal reasons: Van der Waals and electrostatic forces.

276 Eidevåg et al (2020) studied the adhesion of dry snow particles after 90° impact to different wall materials. They considered

277 models for normal direction, tangential sliding, and tangential rolling that account for the adhesive Van der Waals interaction

278 of spherical ice particles (25-275 μm diameter) and their aggregates. The Johnson-Kendall-Roberts (JKR) model for adhesion

279 was used. Their findings showed that the maximum normal velocity at which spherical ice particles adhere to a glass surface

280 decreases with particle diameter. Spherical particles of 100 μm would adhere for speeds less than 0.02 m s^{-1}. In the case of

281 agglomerates with a diameter of 315 μm , composed of 1000 spherical ice particles 25 μm diameter each, the sticking velocity

282 for the adhesion of 90% agglomerates normally hitting the surface increased to 0.5 m s^{-1}, just one third of the Stokes

283 sedimentation speed (1.7 m s^{-1}) calculated for the same aggregate at DC conditions (Tair=-50°C , air density=1.03 kg m^{-3},

284 dynamic viscosity= 1.44E-5 Pa s). These results show that the 300 μm diameter ice particles could stick to the ICE-CAMERA

285 window for Van der Waals' forces alone. Ryzhkin and Petrenko (1997) showed that static charges, naturally transported by

286 ice crystals, increase adhesion. The electrostatic interaction between the ice and the surface is significantly stronger than the

287 van der Waals forces at distances greater than the inter-olecular forces. This effect explains the attachment of the largest ice

288 crystal to the DS of ICE-CAMERA. Once attached to the DS, the weak winds generally observed at DC cannot detach the

289 particles from the DS. Particulates are protected by the boundary layer (BL) that forms on the SD. The 99% thickness of the

290 laminar BL (Blasius solution) at the centre of the DS (0.15 m distance from the window edge) is expected to be 7 mm at -50°C

291 with a wind speed of 1 m/s, decreasing to 2 mm at 10 m/s wind speed. As a result, the particles deposited on the DS are

292 protected against the wind.

3.2 Sublimation of ice particles.

295

296 The DS of ICE-CAMERA is always warmer than the surrounding air. This is necessary to eliminate hoar, enabling the device

297 to be used in all DC conditions. The adverse effect is an accelerated natural sublimation of deposited particles. A wide range

298 of experimental and theoretical research efforts has characterized the effects of temperature and super-saturation on ice crystal

299 growth rates and morphology under conditions relevant to atmospheric processes (for example Lamb and Hobbs, 1971;

300 Libbrecht, 2005; Libbrecht, 2017). The wide variety of ice crystals found in nature has sparked an interest. Sublimation was

301 sometimes regarded either as the opposite process, or a less intriguing process, and was less visited in lab studies.

302 Nelson,(1988) sublimated numerous, 100 μm diameter plate crystals (0.1°C>T>-18°C, 0.05% to 5% sub-saturation) showing

303 that the crystals first lost sharp edges, and finally evolved into spheroidal particles, and the aspect ratio remained almost

304 constant. The sublimation rates were accurately predicted by the diffusion equation with the surface vapour density at the

305 equilibrium value for a uniform surface temperature. The sublimating crystal reaches a self-preserving shape that is one of the

306 shape preserving solutions of the diffusion equation. Ham (1959) showed that ellipsoids and thus spheroids preserve shape

307 during growth and sublimation if the grain surface has a uniform temperature. Jambon-Puillet et al.(2018) also showed

308 experimentally and theoretically that sublimation first smooths out regions of sharp curvature, leading to an ellipsoid. The

309 second stage is the sublimation of the self preserved ellipsoid shape. The entire process may be modelled as a vapour diffusion

310 problem, mathematically equivalent to the resolution of the electrical potential around a charged conductor. Using this analogy,

311 they provided a mathematical method for simulating the sublimation of the ice particle. The sublimation of the ellipsoid turned

312 out mathematically simple, and their method was adopted in this work to numerically simulate the second stage of sublimation

313 of ICE-CAMERA particles.

314 Monodispersed oblate spheroids with an aspect ratio (AR) of 5, in thermal equilibrium with the DS, were assumed in the

315 simulations as a surrogate for ice plates. The two major spheroid axes coincide with the «diameter» of the oblate spheroid, D.

316 In the model, D, DS temperature, air temperature and relative humidity with respect to ice (RHair) can be changed. The

317 sublimation time required for full sublimation of a spheroidal ice particle was computed. As sublimation accelerates when the

318 particle is going to vanish, the time necessary for the complete sublimation is only slightly larger than the time necessary to

319 reduce the particle to the minimum particle size (D=60 μm) accepted by ICE-CAMERA image processing. The simulations

320 assume that the preliminary sublimation of the high-curvature parts of the particle (sharp edges, corners, surface irregularities)

321 was already completed, so that the calculated time of sublimation must be considered as a lower limit for real-world crystals,

322 and probably almost one half of the overall duration of sublimation (Jambon-Puillet et al.,2018). Simulations also assume the

323 thermal equilibrium between the particle and DS, a condition which is not necessarily satisfied on the thermally insulating

324 glass surface of the DS. Figure 9 shows the total sublimation time with the DS heated dT=+20°C above air temperature

325 (sublimation period). The humidity resulted irrelevant in this case, and only results for 70% RHair are shown. Results show

326 that at -30°C air temperature (summer conditions in DC) complete sublimation can occur within a few minutes after attaining

327 the DS sublimation temperature, for all particle sizes up to 1 mm. At lower air temperatures, the sublimation time increases:

328 at -70 °C (winter temperature in DC), particles smaller than 100 μm in diameter still disappear within 10 minutes, while larger

329 particles can survive along the sublimation period. Simulations showed that, at -70 °C, dT should be increased to dT=60°C in

330 order to ensure the complete sublimation of ice particles up to 1 mm diameter during the sublimation period. This is actually

331 not possible with the electric heated window glass adopted, but could probably be achieved by microwave heating.
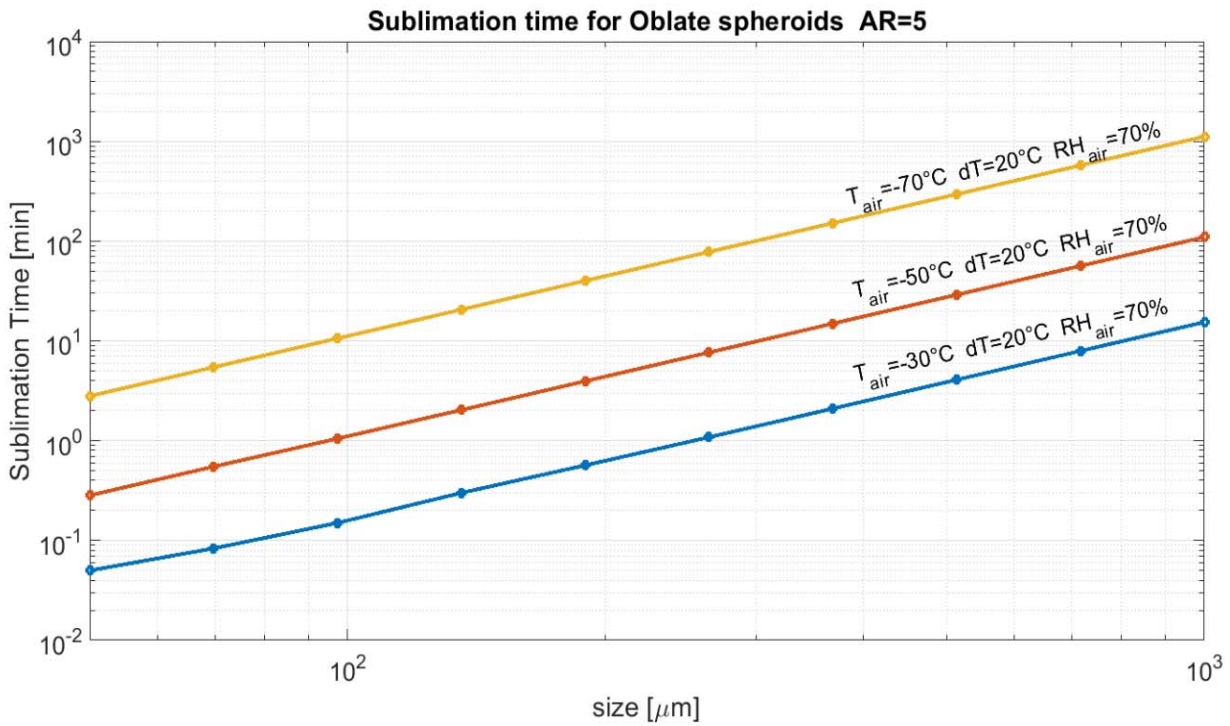
333

334 **Fig. 9: Sublimation time of monodisperse oblate spheroids at varying air temperatures, with dT = 20°C (sublimation**

335 **period).**

336

337 After the sublimation period, most of the particles previously collected on the SD are sublimated, and a new deposition period

338 begins. Even during this period, sublimation still acts on ice particles, albeit slowly. Figure 10 shows the sublimation time

339 expected for monodisperse spheroids during the deposition period. The DS was considered 5 ºC hotter than air. As shown,

340 during the deposition period the relative humidity of air also plays a role, even if secondary. In summer (T_{air}=-30°C),

341 sublimation can take less than a minute for particles smaller than 100 μm and ten minutes for 300 μm particles. During winter

342 (T_{air} = -70°C), all particles are expected to survive through the deposition period. As a rule-of-the-thumb, simulation showed

343 that working with dT=+5°C resulted in an increase of the rate of sublimation by a factor 2-3 compared with a DS in thermal

344 equilibrium with ambient air (dT=0) for the whole range of air temperatures and RH_{air} shown in Fig. 10.

345 Results of Fig.10 show that the effective lower limit of ICE-CAMERA particle detection is not limited solely to the resolution

346 of the optical system and/or image processing software. In summer, particles smaller than 100 μm may be decimated during

347 deposition, unless they fall just before scanning. Such small particles dominate diamond dust events. As a result, ICE-

348 CAMERA, during the summer period, is best suited to the study of cloud precipitation. Nevertheless, visual screening of ICE-

349 CAMERA images showed only a limited number of small particles revealing signs of partial sublimation, such as rounded

350 corners, smooth edges, or a spheroidal appearance. Some small plates (observed mainly in winter, when sublimation during

351 the deposition period is very slow) showed smoothed corners, but it is not clear if this was induced by sublimation or is a

352 natural feature of these ice grains. Also, even in summer, small DD particles such as plates (with no signs of edge smoothing)

353 were normally observed (Sec.6.2). It is probable that most particles (other than, probably, pristine plates) never achieve thermal

354 equilibrium with the DS glass, and that the results of Fig.10 should be considered as the worst case. Also, the sublimation of

355 the high-curvature parts of the particle prior to assuming the spheroidal form (Jambon-Puillet et al.,2018) could take much

356 more time than the sublimation time calculated here for the spheroid. A series of consecutive DS scans at fixed air temperatures

357 is needed to measure the effective sublimation rate of small particles in deposition conditions (dT=+5°C).

358
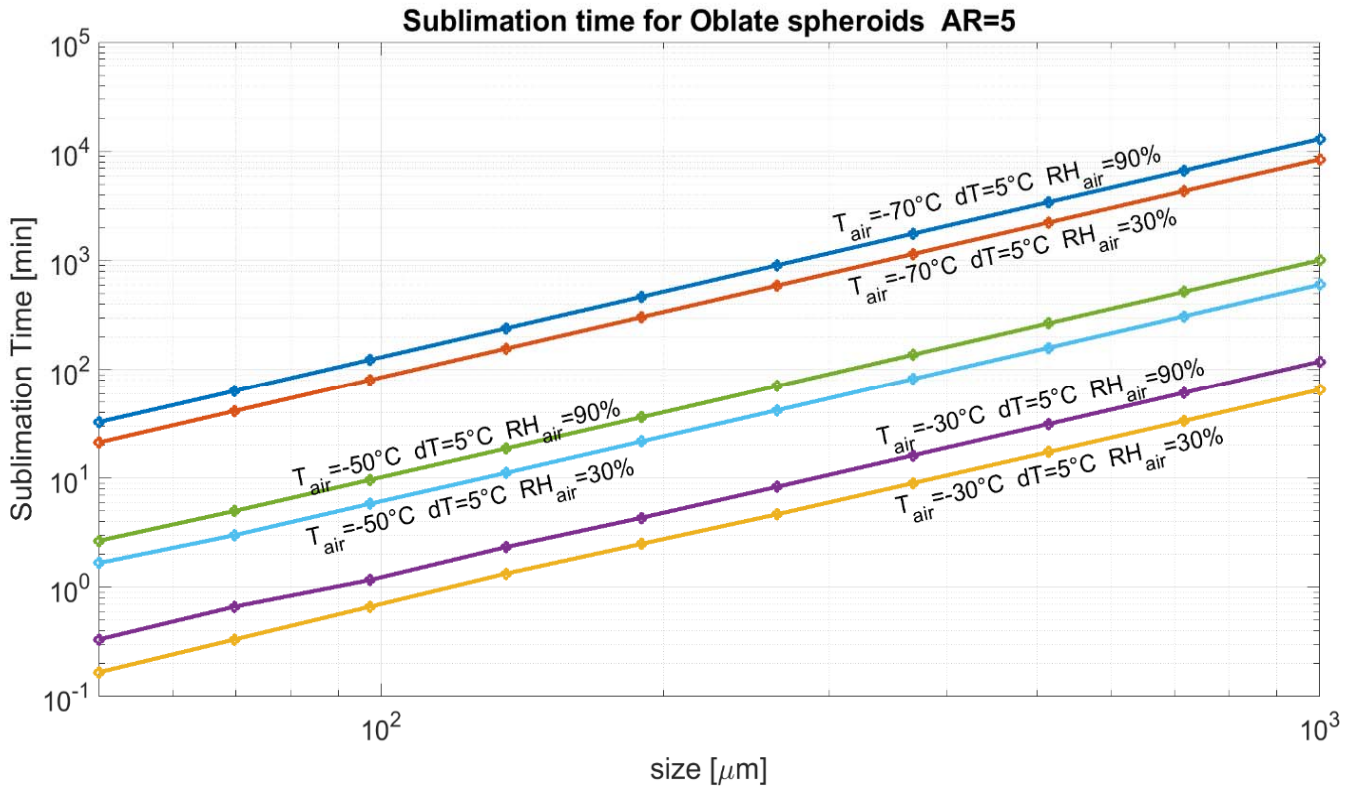
Fig. 10: Sublimation time for oblate spheroids at varying temperatures and air humidity, with a DS temperature of 5°C above air temperature (deposition period).

When a polydisperse particle population is deposited on the DS instead of monodisperse particles, a more complicated sublimation picture arises, because small spheroidal particles, shrinking, are continuously replaced in the size distribution by sublimating, initially bigger ones. An initial uniform particle size distribution (PSD) of the oblate spheroids (AR=5) was assumed with diameters between D=1 and 2000 μm for the simulations. The evolution over time (1 sec resolution) of the PSD was calculated (Fig. 11) in terms of particle survival (the ratio between the actual number of particles in a certain size bin and the initial number in the same bin). No vapour competition between ice particles was taken into consideration in the simulations. Results are similar to those of monodisperse particles (Fig. 9,10), with a slightly longer time of sublimation for polydisperse particles compared to monodisperse particles of the same size. Results for an air temperature of -70°C confirm that most particles larger than 500 μm survive, throughout the DS sublimation period (dT = 20°C), longer than 30 minutes. This means that sublimating by heating the window is quite inefficient for large particles in winter. During the deposition period, at -70°C losses for sublimation are scarce and limited to particles smaller than 200 μm. Consequently, double counting of the same particle (D>500 μm) is possible in two consecutive ICE-CAMERA scans in the cold DC winter. At -30°C air temperature (summer) the heating of the DS with dT=20°C leads to the sublimation of most particles up to 2 mm diameter within 5 minutes. On the other side, during the deposition period particles smaller than 500 μm can undergo sublimation over a period of just 10 minutes in summer, thus limiting the effective period of deposition before a scan. As with monodisperse particles, this introduces bias in the summer because many small particles (typical of DD) can be removed before they are measured.
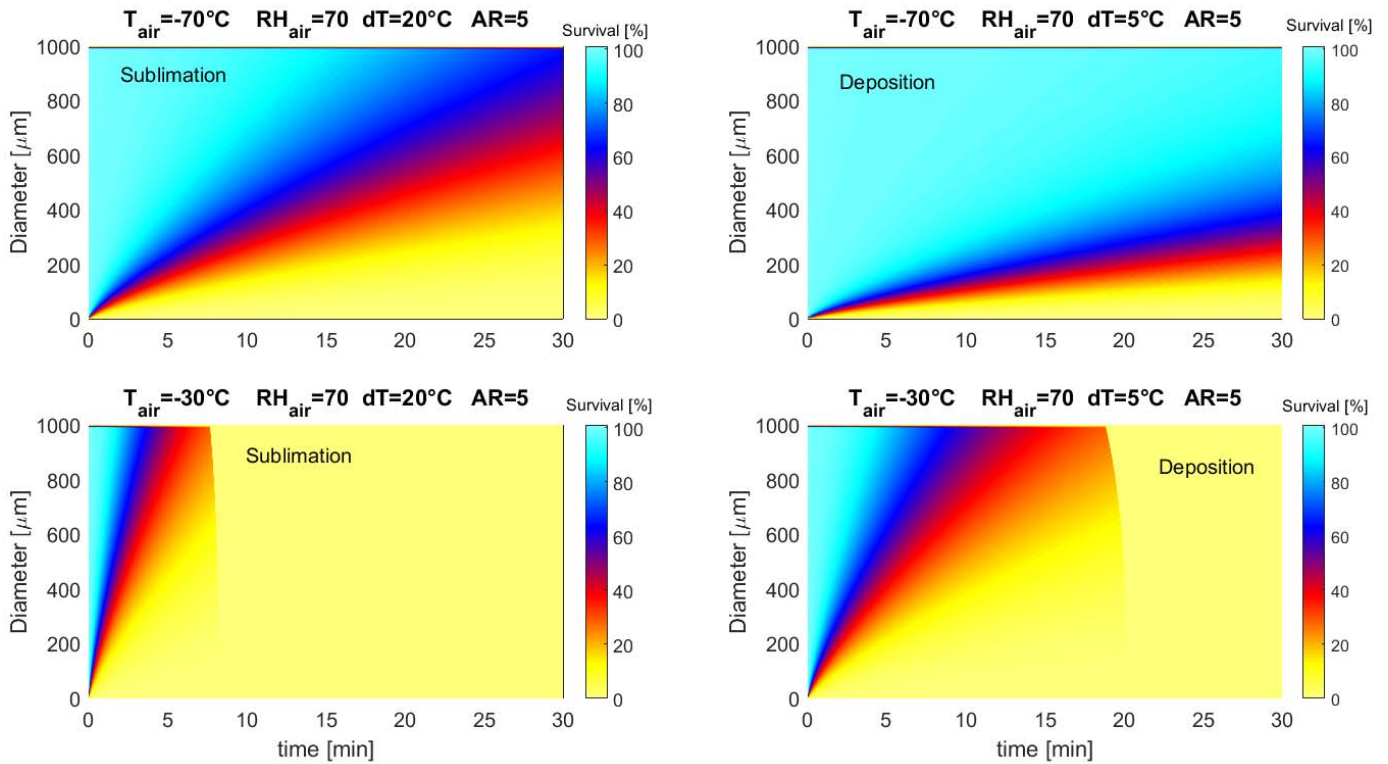
Fig.11: Evolution of a originally uniform PSD of ice spheroids (D=0-2000 μm, AR=5) under different atmospheric conditions. (RHair is a secondary factor affecting the results, shown here for RH=70%). Left: sublimation period; right: deposition period. Top: winter, bottom: summer

Even if these results could be disappointing for interpreting ICE-CAMERA data, the same problems affect the actual method of observing precipitation in DC: Collecting and observing (every 24 hours) the ice particles deposited on flat surfaces ('benches') is affected by the same problem as collecting particles on the ICE-CAMERA DS with dT=0. Fluctuations in relative humidity over 24 hours result in sublimation and regrowth of particles on the "benches" in an almost unpredictable manner. Fig. 12 shows the expected sublimation time for particles (with the same PSD of Fig. 11) placed on 'benches' (or ICE-CAMERA DS) in equilibrium with air (dT=0) for extreme, sub-saturated conditions: winter T_{air}=-70° (RH_{air}=30% and 99%), and summer T_{air}=-30 (RH_{air}=30% and 99%). The PSD evolution is computed with a resolution of 1 sec for a total period of 6 hours. The results show that sublimation also works in winter and with almost saturated air (99% RHair), leading to a complete loss of small particles (D<200 μm) in a few hours. In summer conditions and 30% RHair sublimation happens much more quickly, with the disappearance of all particles up to 2000 μm in 30 minutes. With RHair=99%, sublimation removes all particles in just a few hours in summer. In presence of wind and dry air, sublimation rate could even increase, as observed by Grazioli et al., 2017 in coastal areas. These simulations all refer to sub-saturated conditions: in the case of a 'bench' in thermal equilibrium with super-saturated air, hoar form on the surface, with a possible confusion with precipitation.
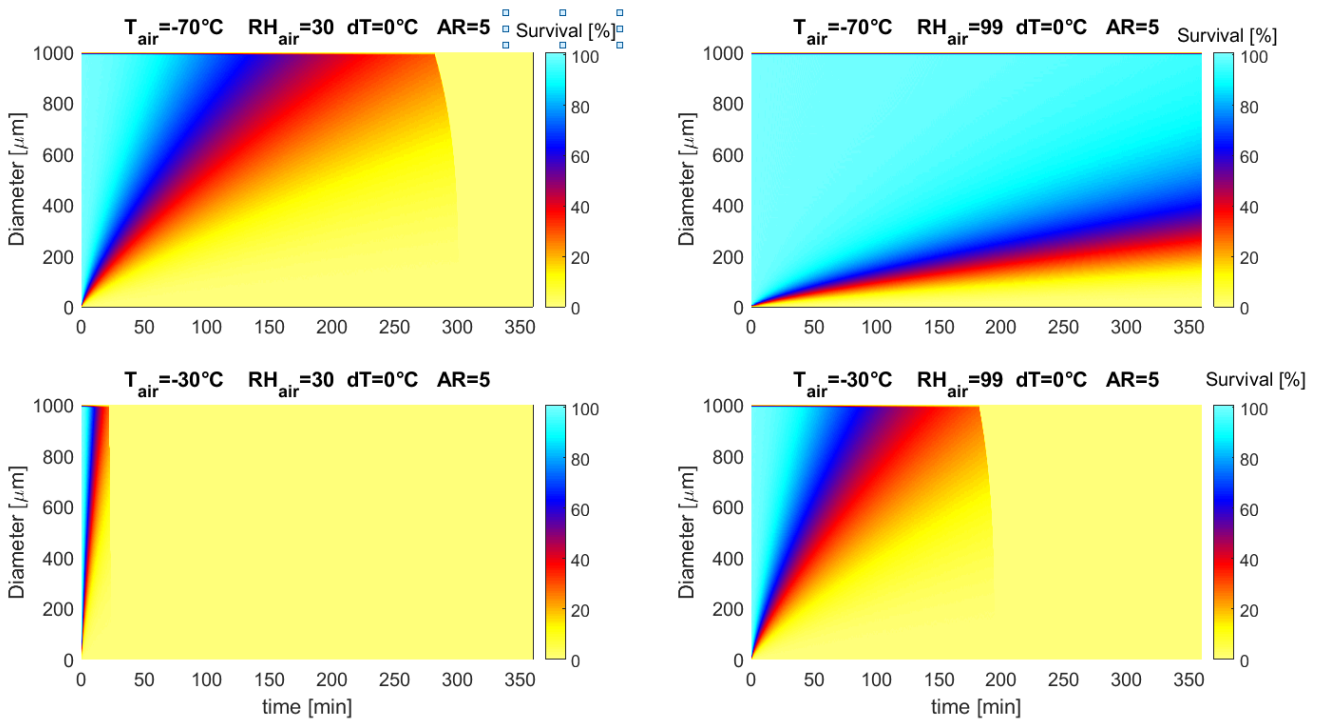
Fig.12: Evolution of a originally uniform PSD of ice spheroids (D=0-2000 μm, AR=5) under different atmospheric conditions. The DS (or 'bench') is in thermal equilibrium with air (dT=0). Top: winter, bottom: summer

4.1. Image processing.

ICE-CAMERA is not just designed to take photographs of ice particles, but to provide automatic morphometry and classification of polar precipitation. This was accomplished through the use of image processing and machine learning techniques. The process is divided into two parts: segmentation and measuring, and classification of ice crystals.

4.1.2 Image Segmentation and Measurement.

After acquisition, the raw ICE-CAMERA scans are segmented, using MATLAB software, to isolate all detected particles. The process follows the workflow of Fig. 13. Refer to Pratt (2007) for image-processing nomenclature, to Walton, 1948 for Feret measurement, to Russ and Brent Neal (2017) for the nomenclature of standard shape parameters such as Eccentricity, Euler Number, circularity, roundness, solidity, compactness, form factor, and number of skeletal branches. The normalized central moments f1...f7 were also computed as described by Hu, (1962).

The Aspect Ratio (AR) is defined as Feret's length/ Feret's width. The Feret-box surface-equivalent diameter (Df) is defined as the diameter of the circle of the same area as the Feret bounding box, while the surface-equivalent diameter (Ds) is defined as the diameter of the circle having the same area as the segmented ice grain.
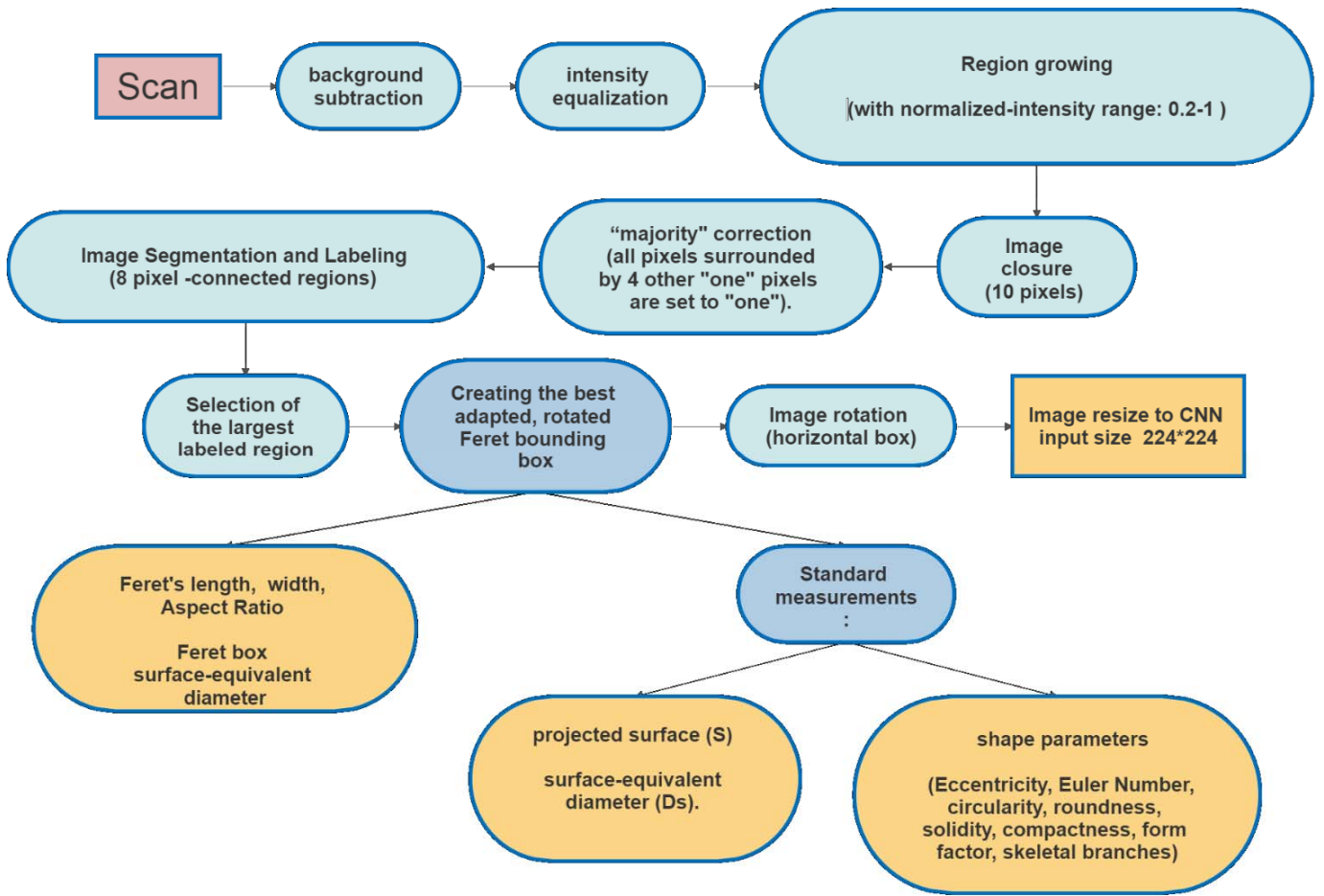
Fig. 13: The image-processing flow chart.

The main steps of Fig. 13 are summarized in Fig. 14 for a rimed, columnar particle
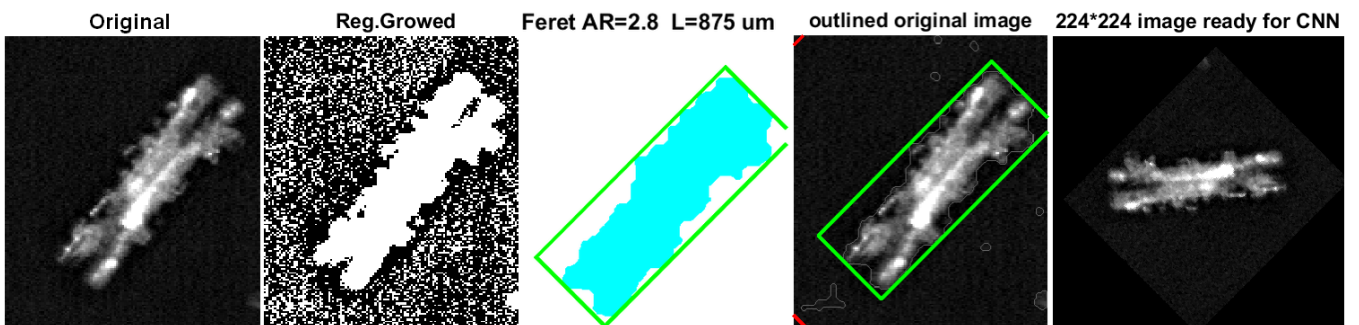
Fig. 14: The original image (in this case a rimed column) is segmented using 'region-growing'. The projected particle area (clear blue) is calculated. The bounding box is determined (green) and the Feret length and width measured. The image is finally rotated to have the mayor axis horizontal, re-scaled, and resized to the CNN input size.

4.1.3 Summary-image of detected particles.

The bounding boxes of all individual ice particles detected in a scan are sorted by Feret length, and reassembled in a summary-image collecting all segmented particles (Fig 15). Each particle is also associated with a numerical record containing the coordinates of its bounding rectangle on the summary-image, shape parameters, Feret size, time of acquisition and local weather data. In this way, the re-analysis of the summary-image is possible instead of re-processing the original, large image. The original image is ultimately removed.
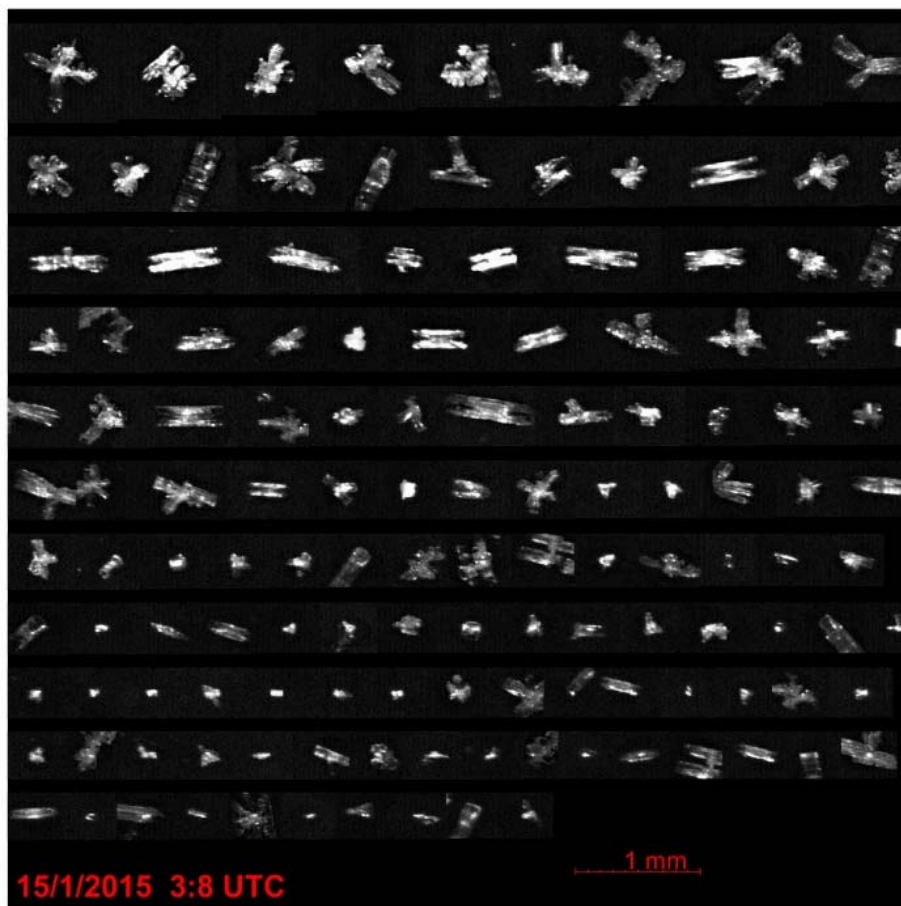
Fig. 15: Example of a summary-image for a single scan.

4.1.4 Limitations and uncertainties in detecting and sizing ice particles.

1) The total number of particles measured is limited to 2000 per scan, as a result of MATLAB memory limitations. Extra particles are not treated.

2) Particles below 3600 μm^2 in bounding-box surface (approximately D<60μm) are not preprocessed (smaller particles could be detected, but most have a seemingly circular shape due to low pixelation or poor focus).

3) The segmentation becomes difficult when overlapping particles or aggregates of particles are present. In such situations, double counting of the same particle may occur in up to 12% in a scan in the presence of an intense precipitation event. The same particles can in fact fall inside different segmented areas of the image, because of the lack, on the original image, of defined boundaries between particles. Overlapping particles are normally classed by the CNN algorithm as "clusters". The Feret measurement of these particles is meaningless. At DC this situation occurs only after heavy cloud precipitation, a relatively rare event.

4) Particles close each other in the original image could be segmented into a single particle by region-growing and thus misclassified.

5) In the case of defocused images, the particle shapes are all close to a fuzzy, round or elliptical shape, which can cause a misclassification into irregular particles, spheroidal particles or plates. ICE-CAMERA images dominated by this type of particles are normally eliminated during a preliminary manual screening. Also, a few big particles in summer resulted rounded by partial sublimation. A few images containing only rounded or "spheroidal" particles of 500 μm diameter or greater were collected during the warmest part of summer, and were manually discarded before the statistical data analysis.

6) Needles and hexagonal plates (typically small, see Fig.26) may be very bright in ICE-CAMERA images due to enhanced light diffusion at preferred angles. For the same reason, hollow columns sometimes have a shiny spot in the middle. .In the case of needles, this effect can reduce the apparent aspect ratio, as the width is apparently increased by the scattered light saturating the camera. For plates, the bright specular reflection blurs sometimes the polygonal contour, especially in the case of small plates.

4.2 Automated classification of ice particles.

An initial attempt at automatic classification of ICE-CAMERA segmented images was made in 2014 using shape factors. This kind of technique has also been used by others (e.g. Lindqvist et al., 2012) for attempting the classification of ice particles. In the case of ICE-CAMERA this approach resulted extremely unreliable. A much more promising approach was offered after 2015 by the rapid development of transfer learning and convolutional neural networks (CNN) (Le Cun et al., 2015; Schmidhuber, 2014). Xiao et al. (2019) successfully applied deep transfer learning to ice particle images obtained with airborne Cloud Particle Imagers (CPI). The CNN approach has added much value to ICE-CAMERA because a reliable classification of ice particles into simplified classes became possible. The CNN used for the ICE-CAMERA particle classification is "GoogleNet" (Szegedy et al. 2015), a variant of the Inception network, a deep convolutional neuronal network developed by Google scientists. GoogleNet is a type of convolutional neural network based on the Inception architecture. It utilises Inception modules, which allow the network to choose between multiple convolutional filter sizes in each block. The GoogleNet architecture consists of 22 layers (27 layers including pooling layers), and part of these layers are a total of 9 inception modules. In this work, GoogleNet was used in MATLAB R2020b environment. The GoogleNet CNN, pretrained on the ImageNet data set (Deng et al. 2009), was used, with its final, fully connected layer changed to size 14. The input layer of the GoogleNet architecture requires images of size 224 x 224.

4.2.1 The CNN classification classes.

Low temperatures and humidity on the high Antarctic plateau reduce the diversity of ice particle shapes. This is observed on the field at DC, at South Pole station (Lawson et al., 2006), and suggested by review works such as Bailey and Hallett (2009). Following an initial survey of the ICE-CAMERA image database, a set of 14 types of particles was selected, as shown in Fig. 16. When choosing the 14 classes, I assumed that shapes easily recognizable by a human operator could also be easily recognizable by a CNN. In the following scheme I tried to fit the classes chosen for ICE-CAMERA with the classification scheme of the ice particles of Kikuchi et al. (2013), an updated version of the original classification of Magono and Lee (1966).

499
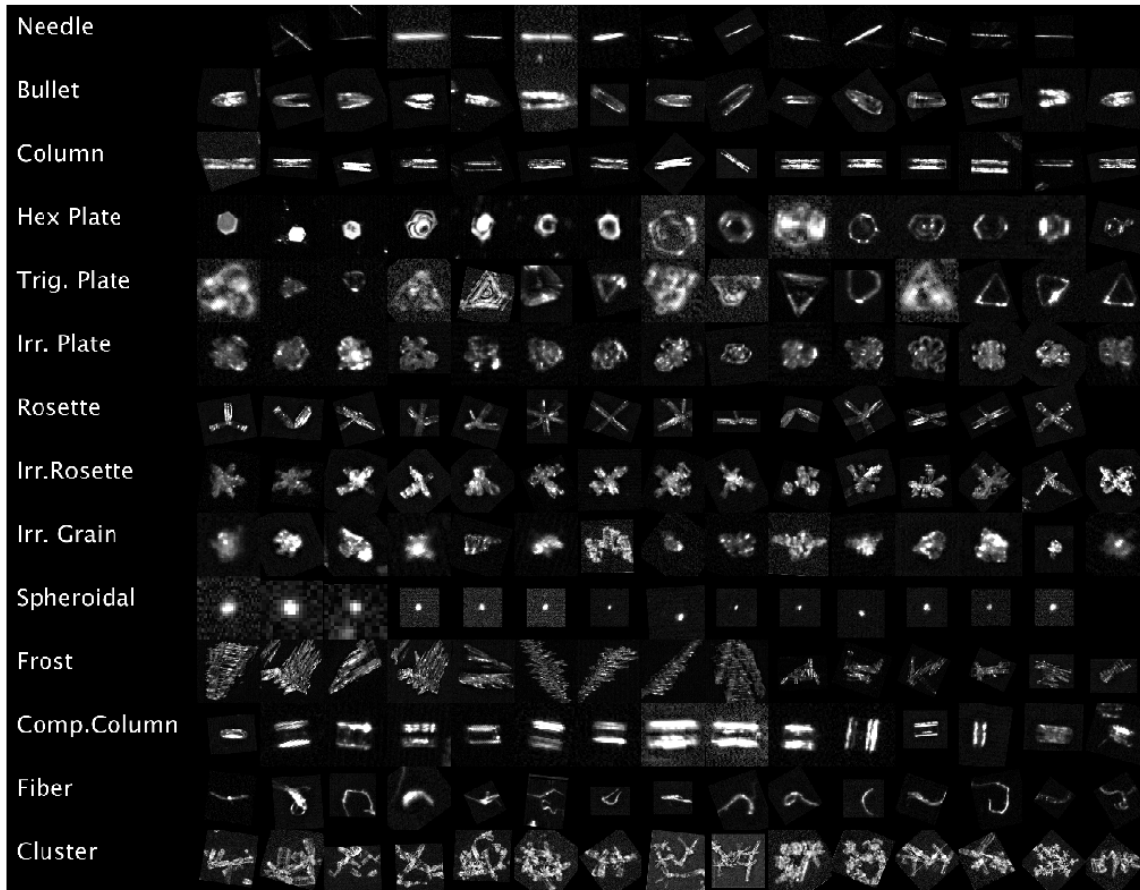
Fig. 16: A sample of ICE-CAMERA images of the 14 classes of ice particles used to train the CNN.

501

502 -**Needles:** covering the classes C1a,C1b,C3d   (Kikuchi et al. 2013)

503 -**Bullets:** covering the C4b-C4c classes.

504 -**Columns:** columns covering classes C2a, R2b, C3a, C3b.

505 -**Hexagonal plates:** covering classes P1a, P1b, P1c, P4f, G2a, G3a, CP3f, CP3d.

506 -**Trigonal plates:** covering the class G2b.

507 -**Irregular plates:** plate-like particles with irregularities, riming, overgrowing plates, etc. But keeping a basic hexagonal

508 shape, covering P6a, P6b, P7a, CP6d, R1b, R2b, R2c, R3a, G4b.

509 -**Rosettes:** bullet-rosettes or column-rosettes, with a minimum of two branches, covering C2c, C3e, C4d

510 -**Irregular rosettes**: rosettes with irregularities, riming, but preserving the typical stellar outline of rosettes. Covering

511 classes P7a,P7b,CP2d ,CP4c,CP5a,CP6e,CP6f,CP6g,R1d

512 -**Irregular grains:** covering CP3e, CP5a, CP6d, G4c,G4a,I3a,I2a,I1a,H1a,H1b

513 -**Spheroidal:** particles with spheroidal or spherical appearence, covering H1a, H1c. (Large particles with D>600μm)

514 detected as 'spheroidal' in DC are usually artifacts caused by defocused images and are not considered in the statistical

515 analysis.

516 -**Compact columns:** short columns covering classes G1a, C3a

517 -**Clusters of particles:** covering A1a, A3a, H2a, H1b, P8b, CP3e, CP5a, CP6h

518 -**Frost**: frost formed on the DS plate CP7,CP8,CP9

519 -**Fibers**: non-volatile fibrous material (from local human activities, Styrofoam particles, textile particles, dust, etc)

520

521 The last two classes are not considered in the statistical analysis of ICE-CAMERA data: they are just used to detect occasional
522 frost formed on the DS, and man-made, non-evaporable (thus persisting on the DS) materials. Uncommon ice particle
523 typologies present at Concordia were not considered in the present work. Trigonal plates have been included, although they
524 are rare, simply because they are seemingly easy to detect with CNN.
525
526 **4.2.3 The training data-set.**
527 For the first CNN training, a set of 5500 ICE-CAMERA segmented images of single particles, sampled randomly from the
528 2014-2017 ICE-CAMERA database, have been manually sorted into 14 image data stores, corresponding to the 14 classes.
529 Fourteen of the computer keyboard keys were marked with the symbols of the 14 classes in order to expedite the manual
530 classification of the initial training data set. These images were used for initial CNN training. The resulting CNN was used to
531 classify the ICE-CAMERA data set for the years 2014 to 2017. The classified images were manually cleaned from incorrectly
532 classified images and added to the 14 training image data stores, as new training images, for a second CNN training. This
533 operation was repeated recursively three times in order to broaden the training database and thus increase the accuracy of the
534 CNN classifier.
535 Figure 17 shows the final number of training and test images selected for each class. The total number of images used for the
536 training was 81800. Trigonal plates were rare, and their number in the training dataset was thus artificially augmented by
537 duplicating the training images, in order to avoid their absence in the small (64-images) training mini-batches.
538
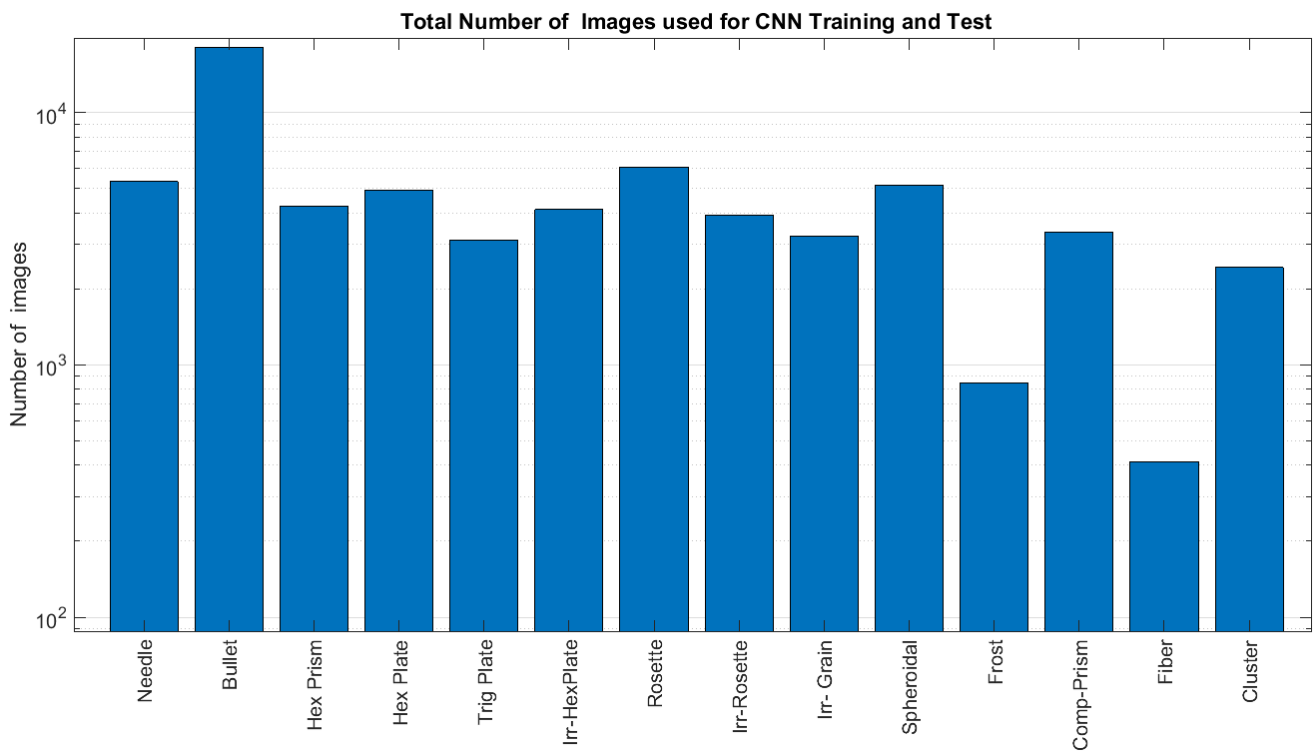
539
540 **Fig. 17: The final number of CNN-training + validation + test images**
541
542
543
544
545
546
547

548 **4.2.4 CNN training details**

549 To meet Google's input requirements, all images of single particles were resized to 224*224 pixels. In the training process,

550 'data augmentation' was applied to the original data set. Artificially 'augmenting' the image data set has been shown to be

551 effective in CNN training (Shorten and Khoshgoftaar, 2019). Images inside each mini-batch are automatically, randomly

552 'augmented' in order to reduce CNN overfitting. The following transformations were used in augmentation:

553 - X, Y reflection

554 - random X, Y translations ±30 pixels

555 - Random scaling 80-120%

556 Other changes such as rotation have not been introduced since the ICE-CAMERA images to be classified are

557 typically oriented horizontally by the image processing procedure (e.g. Fig. 14)

558 The following learning options were utilized in GoogleNet training:

559

560 Solver: stochastic gradient descent with momentum (SGDM)

561 activation: softmax

562 Number of Epochs=5

563 Learn Rate=0.001

564 Batch Size=64

565 L2 weight regularization factor=0.005

566 Validation frequency= every 30 iterations

567 Shuffle of the data set at every epoch

568 10% of the image data set of Fig. 17 was dedicated to validating, 10% for testing, and the remaining 80% of the training. The

569 evolution of the CNN training in terms of accuracy and losses is presented in Fig. 18. The validation line closely tracks the

570 training line, showing the absence of overfitting.
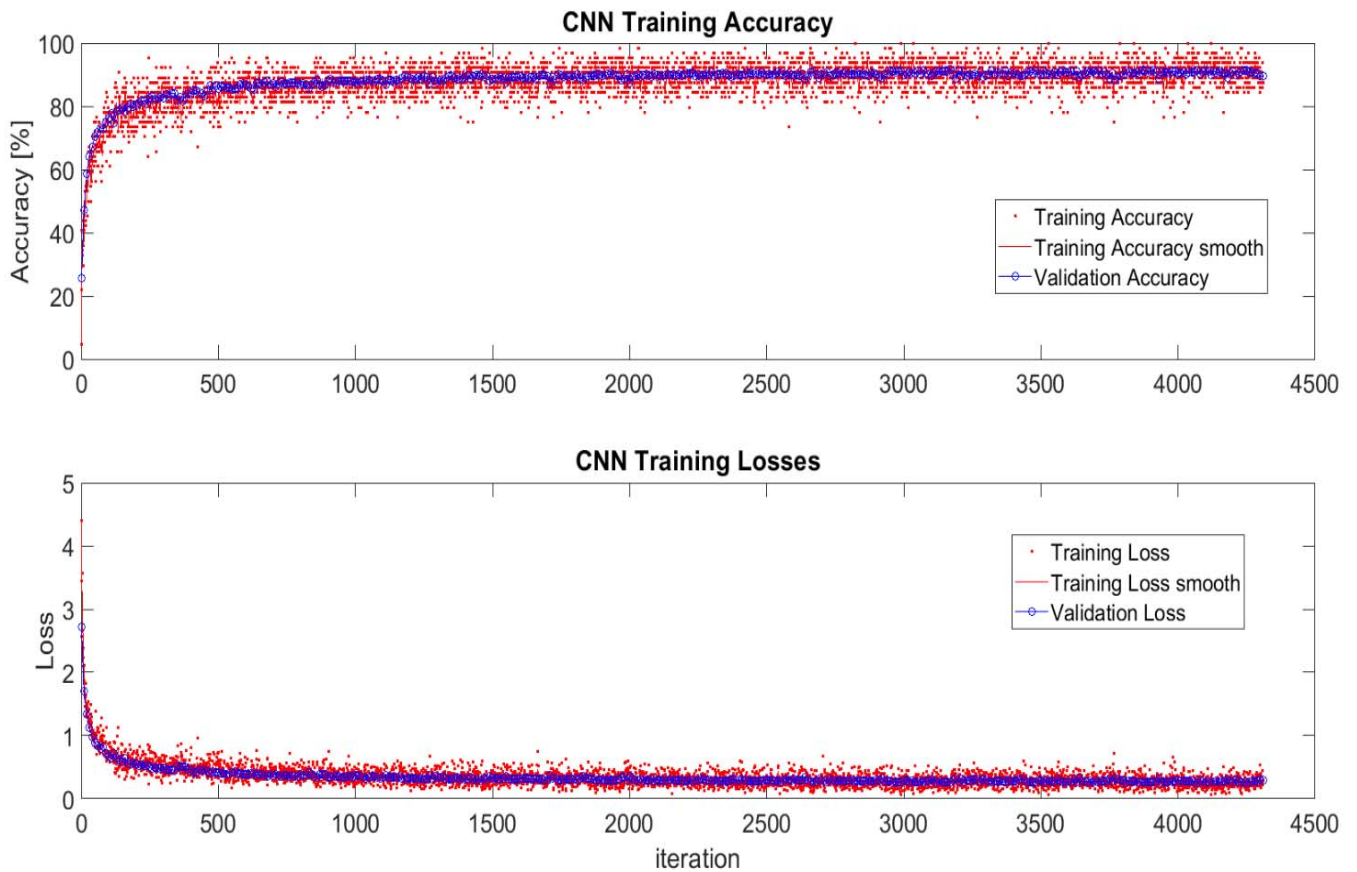
572   **Fig. 18: Evolution of the CNN training.**

573

574   **4.2.5. Testing the CNN classifier.**

575   CNN's performance test results are summarized in confusing matrix graphs like Fig. 19. Each row corresponds to a

576   predicted class (Output Class) and each column corresponds to a true class (Target Class). Diagonal cells refer to correctly

577   classified observations. Off-diagonal cells are improperly classified observations (red color markings increasing

578   misclassification). The column on the far right of the plot shows the percentages of all the examples predicted to belong to

579   each class that are correctly and incorrectly classified (positive predictive value and false discovery rates, respectively). The

580   row at the bottom of the plot shows the percentages of all the examples belonging to each class that are correctly and

581   incorrectly classified (true positive rate and false negative rate, respectively).

582

583

584

585

586

587

588 **4.2.6 Accuracy of the classifier**.

589 In the column-normalized summary (Fig. 19), the percentages along the i-th column shows the probability (P) of a "true"

590 particle in class i-th being classified in each of the 14 output classes.
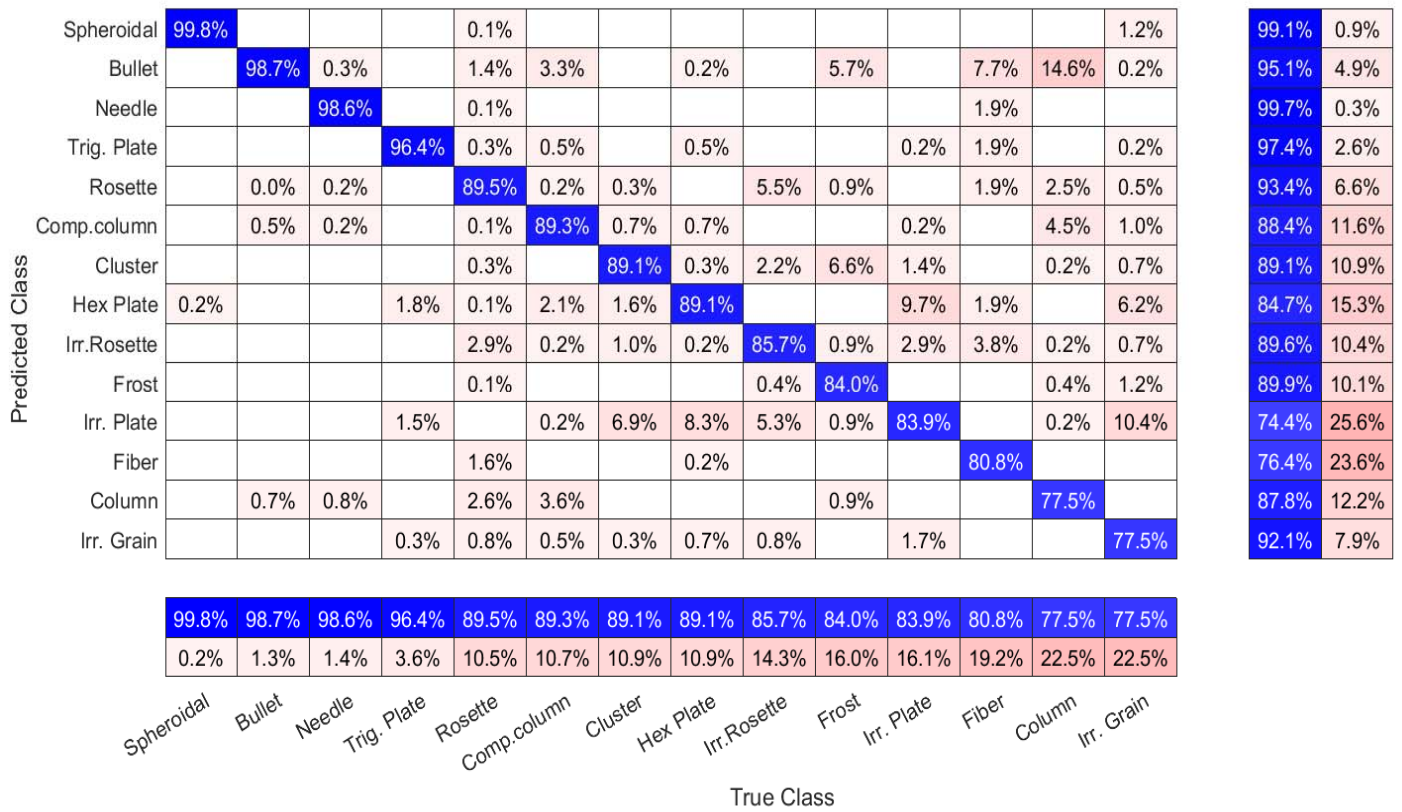
591

592 **Fig. 19: Confusion plot of the CNN (column-normalized)**

593

594 Reading the columns from left to right, the accuracy of the CNN in properly classifying a particle belonging to the i-th true

595 class (bottom row) can be assessed. The results are summarized below:

596

597 -Good accuracy (P>90%) in identifying needles, spheroidal, bullets, trigonal plates.

598 -Compact columns are misclassified into columns (3% of the time) and bullets (3% of the time).

599 -Hexagonal and irregular plates are confused approximately 10% of the time. This is expected since the edges of the plates

600 (usually small) are sometimes blurred in the image.

601 -Irregular rosettes are misclassified in 5% of cases as pristine rosettes and in 5% of cases as irregular plates.

602 -Irregular plates are confused with hexagonal plates 10% of times.

603 -Irregular grains are sometimes mistaken with irregular plates (10%) and hex plates (6%).

604 -Columns are misclassified as bullets 15% of the times.

605

606 The three-dimensional structure of the ice particles is lost in the ICE-CAMERA images, so that some thick ice forms such as

607 C4a, P1b, G3b, CP1a, etc. (Kikuchi et al, 2013), if any, are likely to be misclassified by this CNN.

608

609

A different view to read the CNN test is the row-normalized summary of the confusion matrix (Fig. 20).
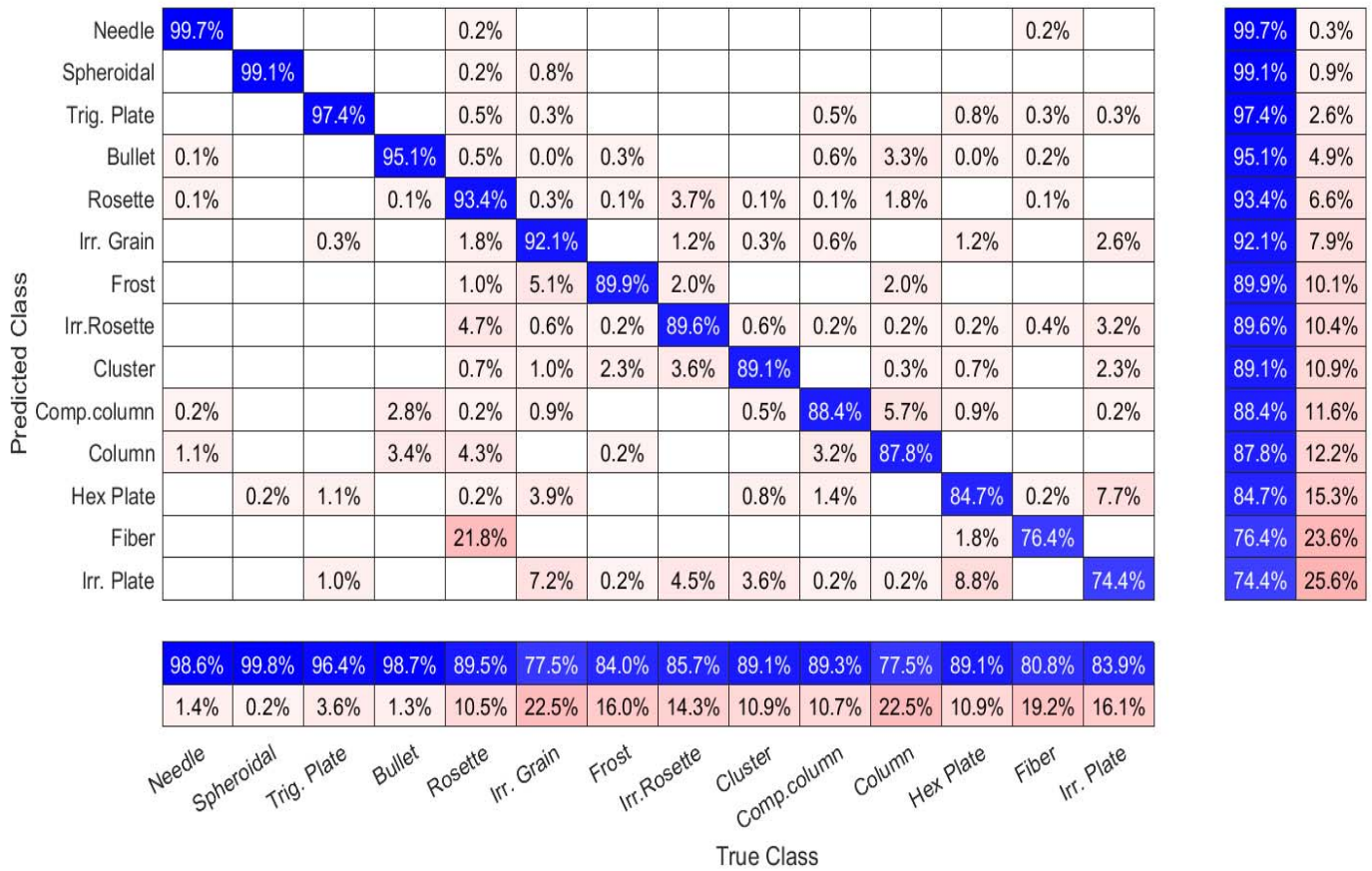
Fig. 20: Confusion plot of the CNN – (row-normalized)

Percentages along the i-th row now show the probability for a particle classified into the i-th class to effectively belong to each of the 14 true classes. Reading the rows of Fig. 20 from top to bottom, results are:

-Particles classified as needles, spheroidal, trigonal plates, bullets, pristine rosettes and irregular grains effectively (P>90%) belong to their class.

-Particles classified as irregular rosettes have a 5% chance of being regular rosettes

-Particles classified as compact columns have a 6% chance of being columns.

-Particles classified as columns have a 4% chance of being a 2-branch rosette and 3% of being bullets or compact columns.

-Particles classified as pristine plates have a 4% chance of being irregular grains.

-Particles classified as irregular plates have a 7% chance of being irregular grains, 8% regular plates, and 5% of being irregular rosettes

6.1 Overview of ICE-CAMERA data set.

From January 2014 to December 2021, ICE-CAMERA has segmented a total of 11.007.543 particles. This gross count includes particulates successively rejected for the statistical analysis. The distribution of the number of particles observed in the course of the months is illustrated in Fig. 21. In some months, errors in ICE-CAMERA or processing software contributed to the small numbers observed.
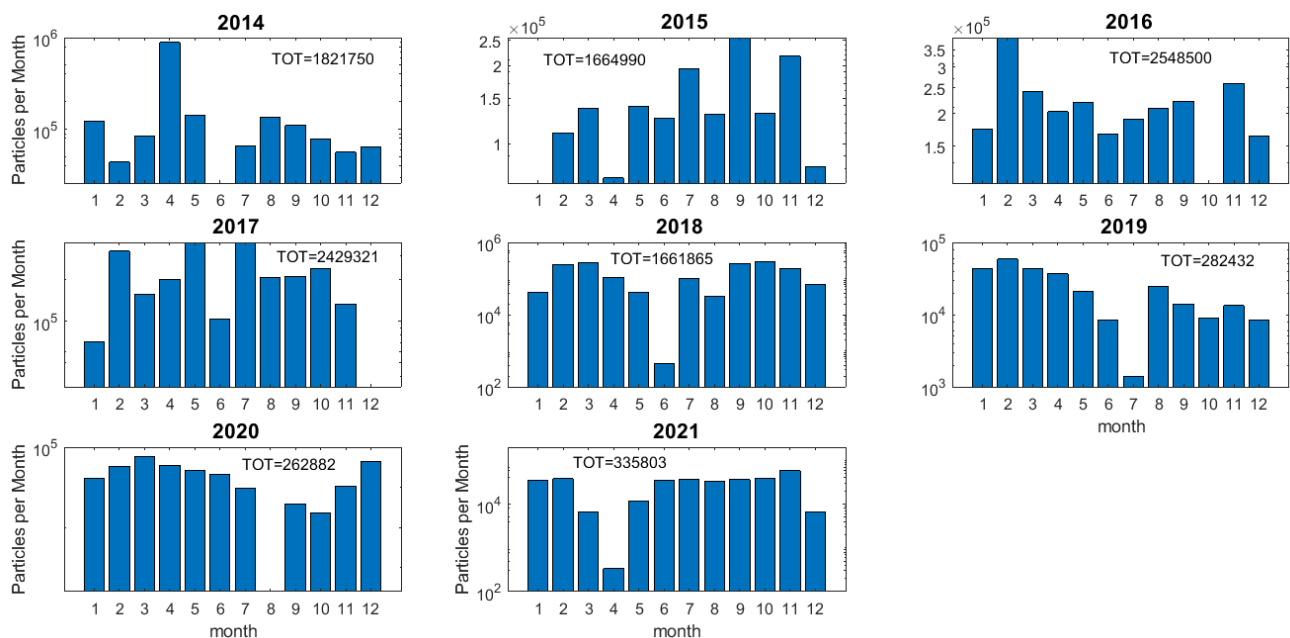
631 **Fig. 21: Ice particle count statistics per month for the years 2014 to 2021. The total number per-year is also indicated.**

633 The number of particles per scan (NpS) is a rough indicator of the intensity of the collected precipitation, but it could be
634 affected by sublimation, because in condition of 'warm' air the smallest particles could disappear from the DS before being
635 detected (sec.3.2). Figure 22 shows the NpS in relation to the air temperature for the whole period 2014-2021, in box and
636 whisker format. On each box, the middle mark indicates the median, and the lower and upper edges indicate the 25th and 75th
637 percentiles, respectively. The lower and upper whiskers indicate an interquartile below the 25th percentile and an interquartile
638 above the 75th percentile.

639 Most ice particles were detected at temperatures between -60°C and -45°C, characteristic temperatures in spring and autumn.
640 The NpS at -70°C is not statistically different from the NpS at -30ºC. This result suggests that sublimation on the SD during
641 the deposition period is less important than the natural variability of precipitation in determining the number of particles
642 detected during the acquisition.

643
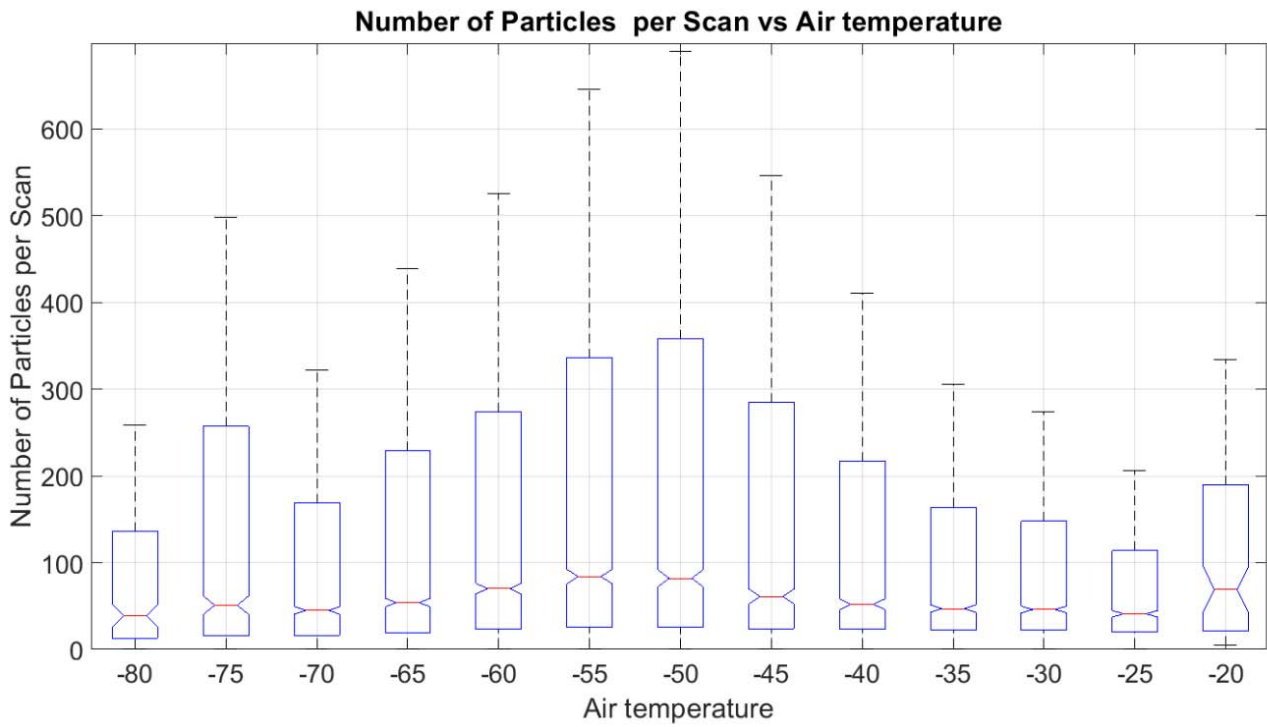
Fig. 22: Statistics of NpS as a function of air temperature for the period 2014-2021

645

646 The same consideration can be deduced when considering the statistics of NpS with relative humidity (Fig. 23). Most particles

647 were detected with relative humidity ranging from 35% to 60%. NpS at 20% HR does not differ statistically from NpS at 80%

648 RH. Even if RH is less important than temperature in determining the sublimation rate, also this result suggests that

649 sublimation does not affect dramatically the *number* of particles finally detected by ICE-CAMERA.

650

651

652
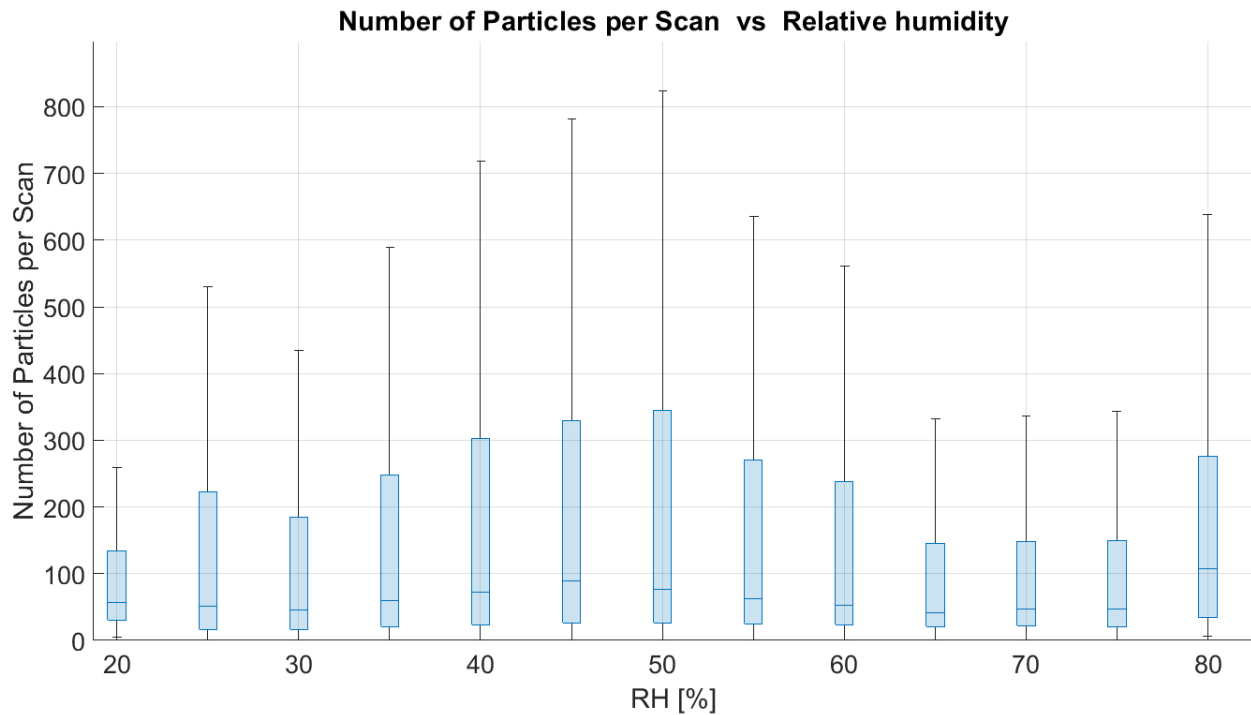
Fig. 23: NpS statistics based on RH for the period 2014-2021.

654

655 Figure 24 shows NpS in relation to wind velocity. Ice particles were collected by ICE-CAMERA under all wind velocity

656 conditions encountered in DC. Ice particles were numerically more abundant when the wind was between 7 ms^{-1} and 16 ms^{-1}.

657 As the average surface wind speed at DC is around 3≈4 m s^{-1} , particles were collected on the DS preferentially with winds

658 stronger than the average, a condition typically encountered in winter (Argentini et al.,2014). These winds exceed the threshold

659 value of 5 m s^{-1} for blowing snow at ICE-CAMERA altitude, and may ultimately contain drifting snow. The drop of NpS for

660 the highest wind speeds (rare in DC) is probably due to the limited attachment of snow to the DS.

661
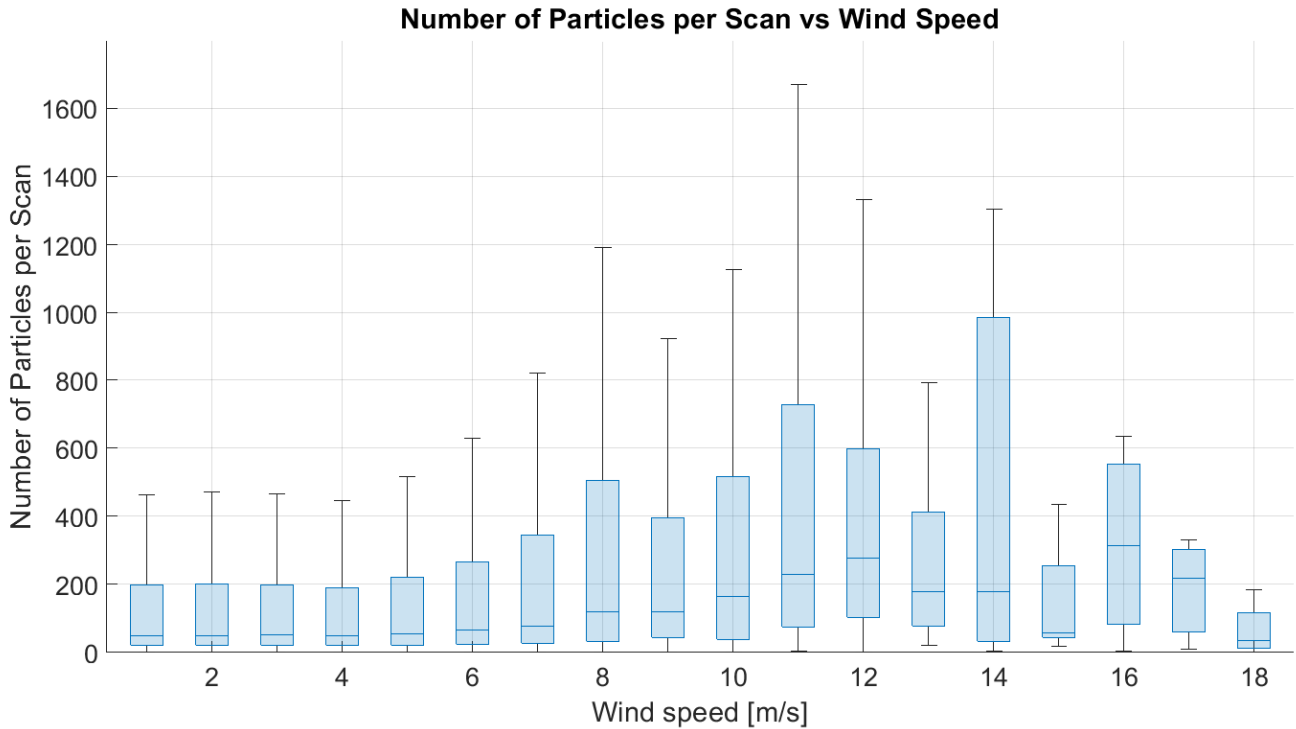
662

663 **Fig. 24: NpS statistics in terms of wind speed for the period 2014-2021.**

664

665

666 **6.2 Image processing and CNN used on ICE-CAMERA data.**

667 MATLAB post-processing software, including the CNN classifier (Sect.4.2) and measurement tools (Sect.4.1) has been

668 applied to the 2014-2017 ICE-CAMERA dataset. Even if the detailed analysis of these data is the task of a separate paper, a

669 sample of the capacity of the instrument is presented in this section for the first two years of measurement (2014-2015). The

670 total particles analyzed resulted in N=553.358. The number of particles classified in the 14 classes is reported in Fig. 25. The

671 relative rarity of trigonal plates and spheroid particles is evident.
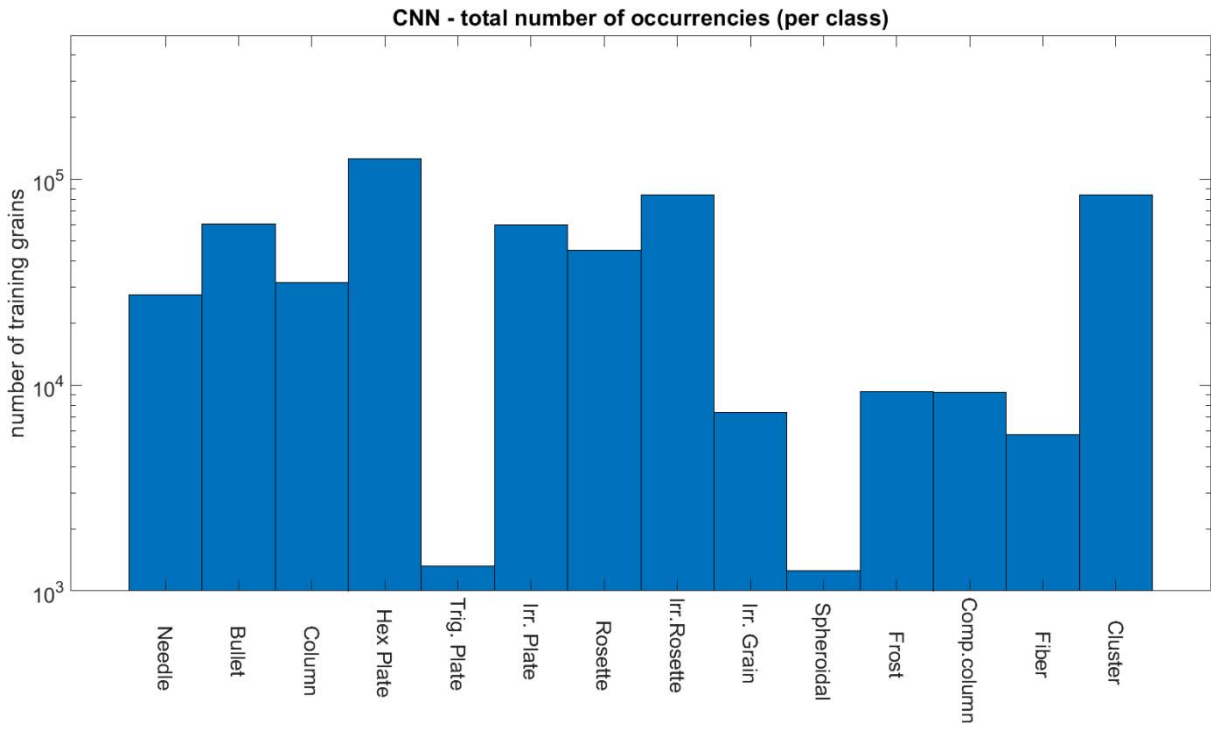
Fig. 25: Particles classified in the 14 classes for years 2014-2015 .

Figure 26 shows the Feret length statistics in box and whisker format. Particles classified as plates, needles, compact columns, spheroidal and irregular grains gave an average length lower than 300 μm. Bullets and columns mean length resulted in the 400-500 μm range, while for rosettes and irregular rosettes was in the 350-550 μm range.

682
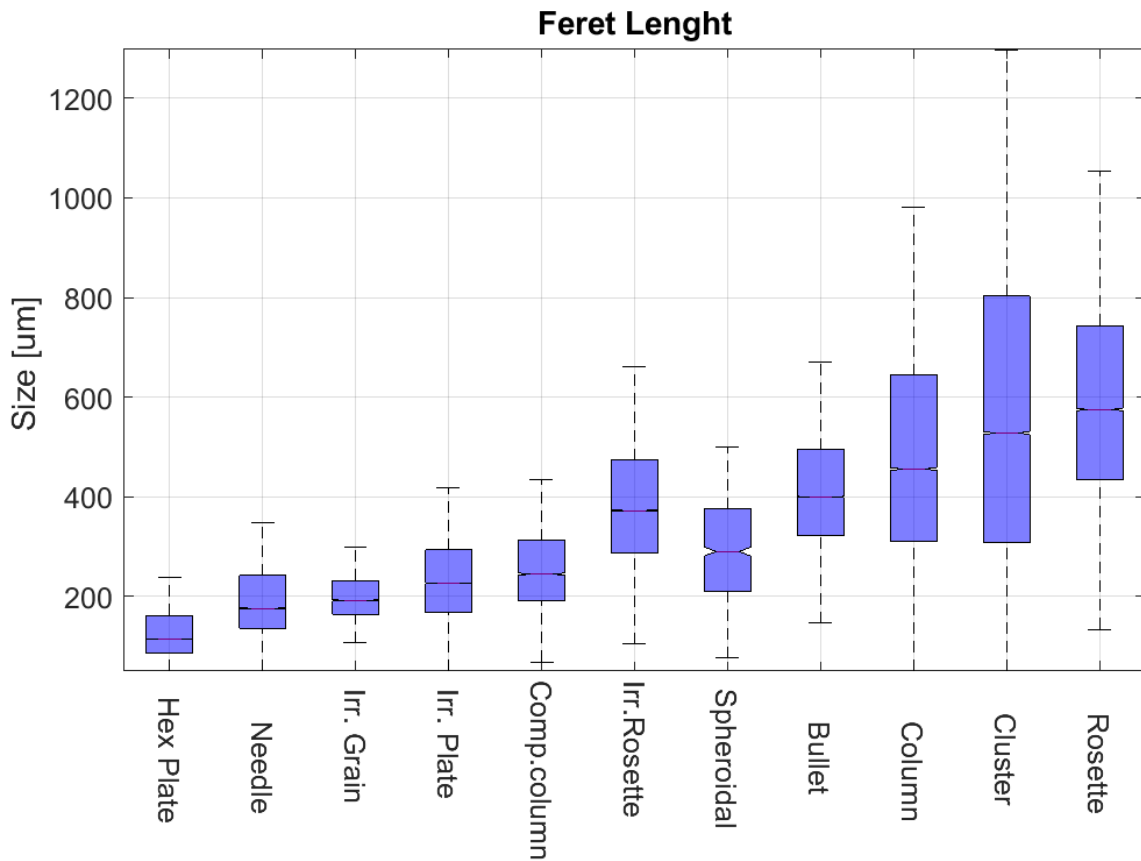
684   **Fig. 26: Feret length statisticsfor the years 2014-2015**

685 Figure 27 shows in detail the probability distribution of the Feret length for plates and rosettes. For plates, the peak of the

686 distribution is for Lferet=100 μm, similar to the peak of the diamond dust (maximum) size distribution measured by Lawson

687 et al. (2006) at SPS in summer. It must be pointed out that Lawson et al. (2006) measured also particles as amall as 30 μm ,

688 while particles below 60 μm are not processed by the ICE-CAMERA software, and are therefore missing from the probability

689 distribution. This finding indicates that the possible sublimation of particles less than 100-200 μm during the deposition time,

690 suggested in Section 3.2, is not relevant for the final particle size statistics. The results obtained from ICE-CAMERA for

691 pristine rosettes differ considerably from those of Lawson et al (2006), because the peak of the probability distribution resulted

692 L=480 μm, to be compared with L=120 μm of Lawson et al (2006). This difference is not explicable with the eventual

693 sublimation of the smallest rosettes on the DS. Instead, this result is a realistic feature, sustained by the direct visual observation

694 of rosettes in DC precipitation.

695
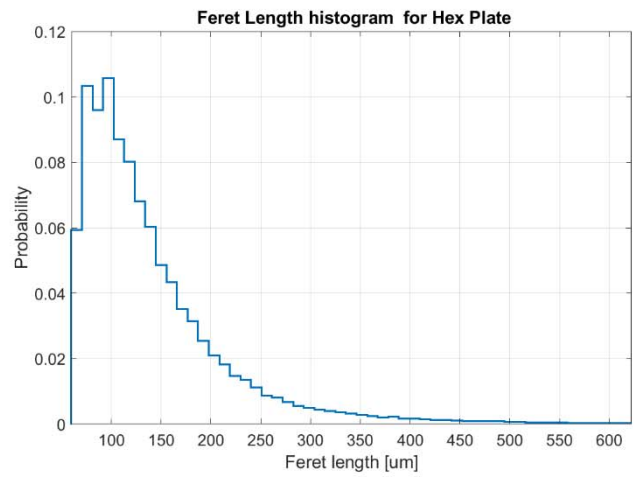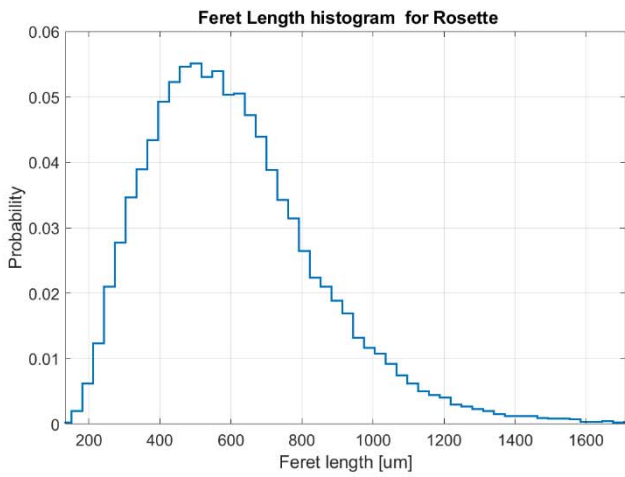
Fig. 27: Feret length probability distribution for rosettes and regular plates. The important presence of small plates (D<200µm) suggests that sublimation on the DS is not relevant. years 2014-2015

Figure 28 shows the trend of the mean Feret length of hexagonal plates with air temperature (sample size=121166 plates). The maximum plate size is observed at temperatures of -30 to -40°C. If sublimation on the DS dominated the size distribution of the plates observed after a DS scan, an inverse relationship between size and temperature would be expected. This finding again suggests that sublimation on the DS (even in summer, and up to -30°C air temperature) is not as important as numerical simulations might suggest.

704
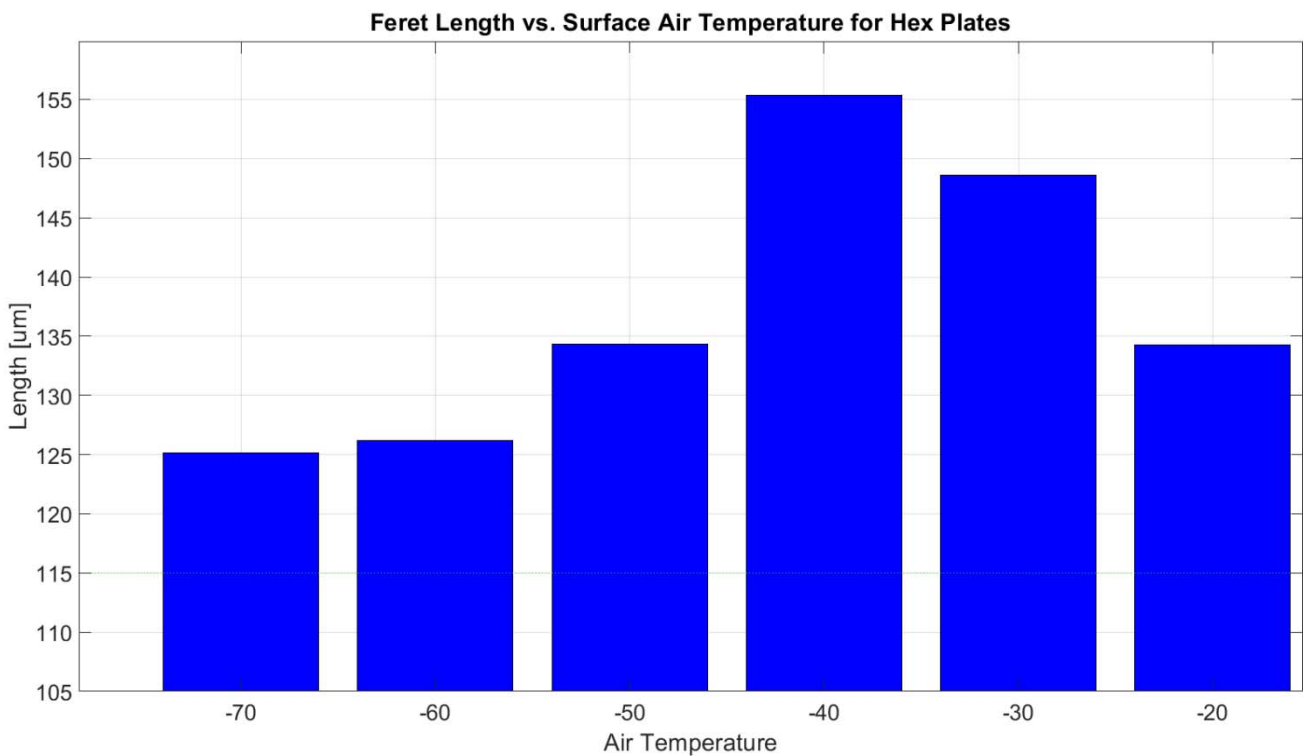
Fig. 28: Average plate length with respect to air temperature – years 2014 to 2015.

706

707 Figure 29 shows Feret's aspect ratio per class. Not surprisingly, many "rounded" classes (plates, rosettes, etc.) have an AR<2.

708 Compact columns show a median AR close to 2.4, while columns and bullets are close to 3. The average AR for the needles

709 was 3.2, which is lower than expected for the reasons outlined in section 4.1.4.
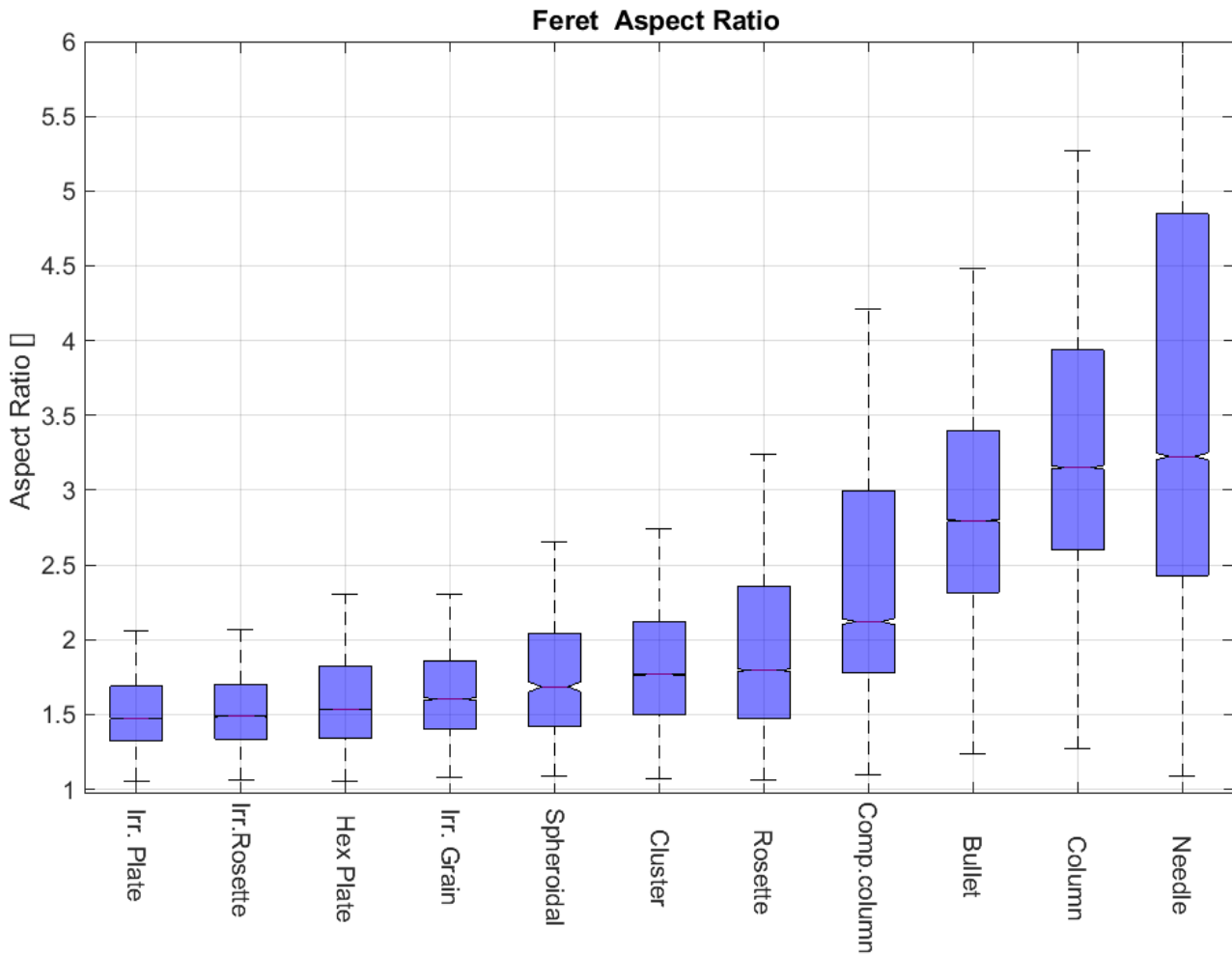
710

711 **Fig. 29: Aspect Ratio statistics for the years 2014-2015**

712

713 Figure 30 shows the surface-equivalent diameter Ds of the particles. Figure 31 shows the ratio between the surface equivalent

714 diameter (Ds) and the bounding box equivalent diameter (Df). The difference between the two diameters is relevant for "fluffy"

715 particles like rosettes and clusters. For those particles, Ds/Df gave values of 0.6 to 0.65. For comparison, a round particle is

716 expected to have a ratio of Ds/Df=0.78.
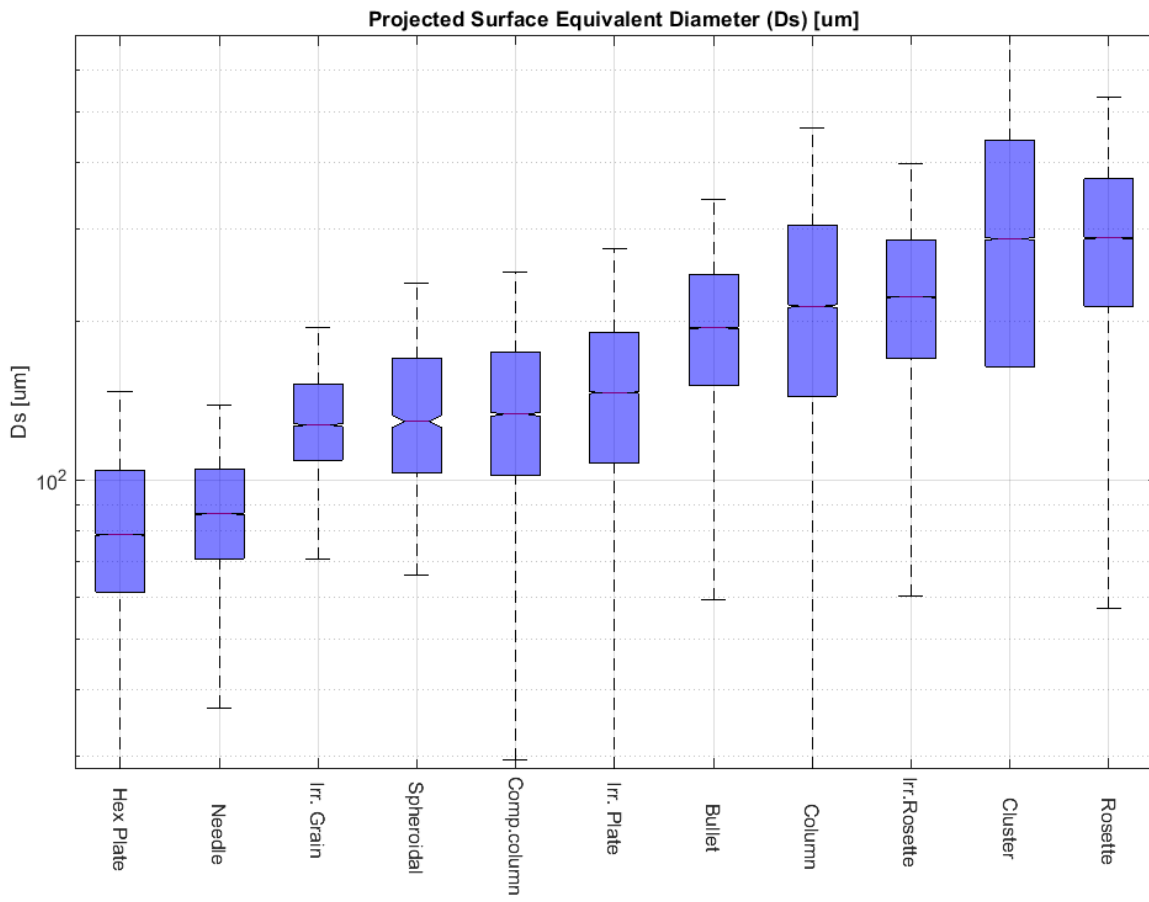
717

718   **Fig. 30: Projected surface-equivalent diameter (Ds) for the years 2014-2015**

719
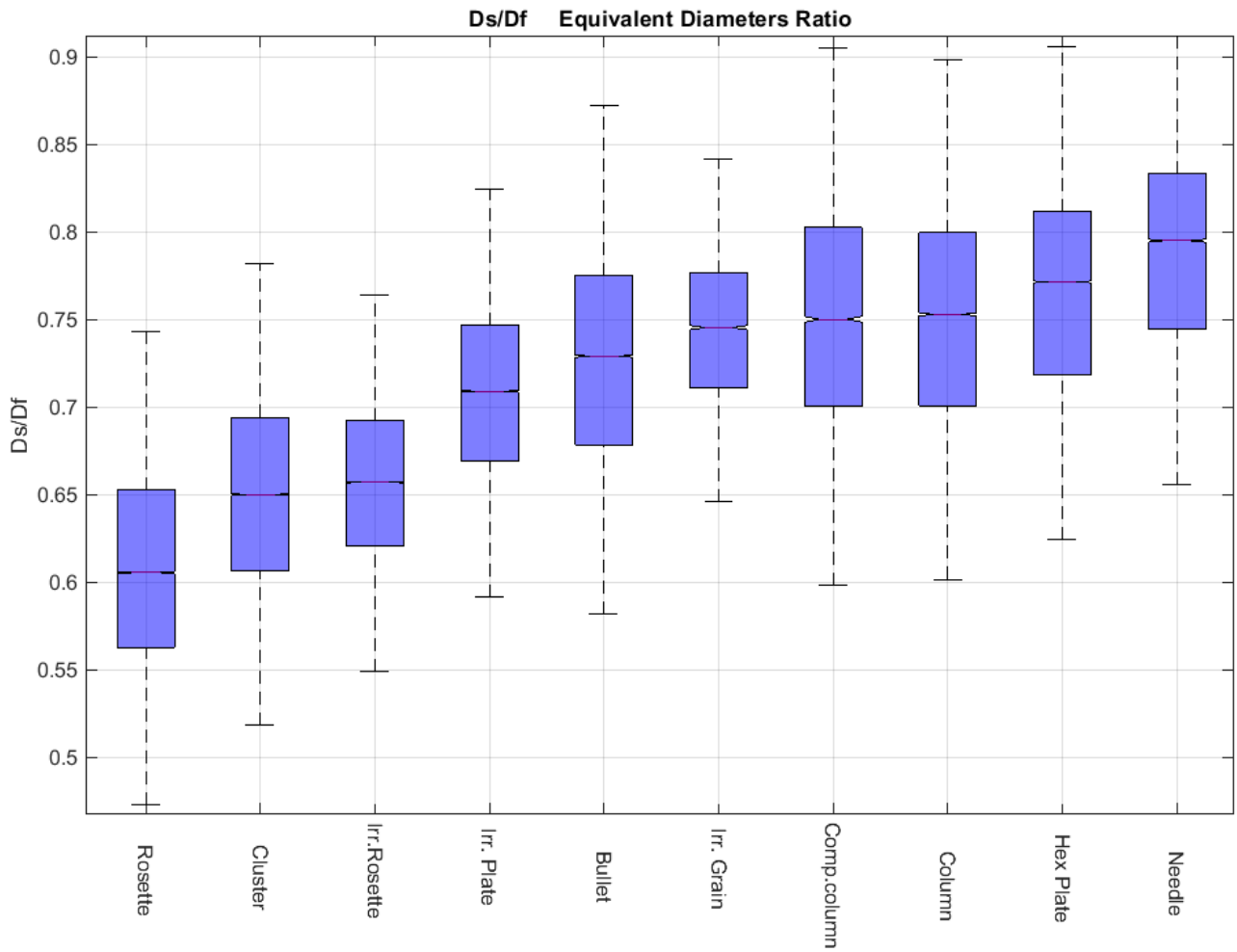
Fig. 31 Ratio between surface-equivalent (Ds) and Feret box-equivalent (Df) diameters - years 2014-2015

720

721

722

723

724

725

726

727

728

729

730

731

6.Conclusions.

ICE-CAMERA, although very similar to a simple flatbed scanner in its basic design, has represented a technical challenge for its implementation at DC. Hardware and software have been continuously and extensively modified at DC over the past five summer campaigns. The result is now a reliable instrument, running throughout the year on an hourly basis, for the statistical study of precipitation in internal polar areas. Particle size and morphology are automatically obtained, and some semi-quantitative precipitation estimates can be derived. The collected data are automatically pre-analyzed, but they can be post-processed at any time, in order to follow the continuous improvements of the image processing and machine learning algorithms. The GoogleNet CNN, trained specifically for this instrument, has succeeded in classifying ICE-CAMERA images into 14 form classes, with an accuracy of more than 80% for most of them. The instrument is particularly useful for automatically measuring the size of individual ice particles in precipitation, a process virtually impossible manually, and certainly impossible on the field in DC and elsewhere on the Antarctic plateau in winter. ICE-CAMERA scans are carried out every hour. Keeping the surface of the instrument free of frost all the time and cleaning it by heating the deposition surface after each scan is paid with the possible loss of small ice particles. Particles less than 100-200 um can disappear by sublimation before being recorded, especially in summer. This problem is complementary to the problem encountered when observing precipitation manually: when observing precipitation manually every 24 hours, (as is the case of DC) the reprocessing of particles, or the formation of ice and hoar artifacts cannot be prevented. In ICE-CAMERA, frost and ice regrowth are suppressed, but small particles may disappear for sublimation. ICE-CAMERA data, collected since 2014, have already been statistically processed and the results will be described in a specialized paper. Results from a subset of data (years from 2014 to 2015), was presented in this work. These results demonstrated the capability of the instrument to classify and size individual ice particles in DC precipitation, apparently without dramatic losses of small particles for sublimation . Cloud precipitation particles (rosettes) were found to be significantly larger (480 μm) than those observed at SPS by Lawson et al (2006), while plates resulted of similar size (120 μm). Unfortunately, only non-polluted, very cold, low humidity, low precipitation environments (like high mountain tops, dry polar environments) could house a similar instrument. In the presence of pollution, marine aerosols or dust, manual cleaning of the DS would be required to remove solid particles and salts escaping sublimation. For coastal zones, the temperature is generally close to zero, making the thermal cleaning of the DS by sublimation problematic. In these environments, if an instrument like ICE-CAMERA were installed, a mechanical wiper would replace the heated window of the current instrument. Furthermore, the CNN presented in this paper should be re-trained with different classes of ice crystals.

7. Technical issues.

Using ICE-CAMERA at DC, as well as other automated instruments, was difficult. The instrument had several failures along years, and each one was difficult to fix, at least in winter, when the instrument had to be dismounted from the roof of the shelter at -70°C and eventually fixed in the local lab by the winter-over crew, with remote assistance from Europe. Until a few years ago, communicating with DC was limited to email with small attachments, making remote assistance a lengthy task. Even today, connecting the rest of the world remotely with the ICE-CAMERA PC, to operate on the instrument software, is virtually impossible. Most hardware failures in DC were due to software bugs or computer failures. Rather than having trouble with low temperatures, operating in DC means dealing with limited heat-dissipation of PC parts such as power supply and hard disks, electrostatic discharge issues in low-humidity, heated environments, lack of spare parts for most of the year, a variable skill-ness of winter-over personnel. Failures in the thermal control of ICE-CAMERA caused some mechanical stress and failures in the focusing sledge, while water condensation eventually rusted the bearings of the stepper motors (all bearing were de-greased for a better low temperature operation). The CNN used to classify ICE-CAMERA images is continually changing and improving and the CNN training data set increases with time, as new images collected by ICE-CAMERA are used as new training ones.

Code and Data availability.

 The CNN developed as part of this work (under Mathworks MATLAB R2020B), along with the image data set (224*224 images for the 14 classes of particles) used for training, validation and testing the CNN are available at ZENODO repository (Del Guasta, 2022)

Acknowledgements.

I am grateful to the Italian Antarctic Project PNRA for supporting this work with the projects ICE-CAMERA (PNRA 2009/A4.1) and PRE-REC (PNRA 2013/AC3.05). I am also grateful to the 'Osservatorio Meteo-Climatologico Antartico' (PNRA 14_00100) for the Meteo data, and to all the logistics staff and winter-over crews of Concordia station, all working hard to permit our scientific activity. I am also grateful to Francesco Castagnoli (INO CNR) for the initial design of the instrument.

References.

Aristidi, E.: An analysis of temperatures and wind speeds above Dome C, Antarctica, Astronomy and Astrophysics, 430, 739–746, https://doi.org/10.1051/0004-6361:20041876, 2005.

Argentini, S., Pietroni, I., Mastrantonio, G., P., V. A., Dargaud, G., and Petenko, I.: Observations of near surface wind speed, temperature and radiative budget at Dome C, Antarctic Plateau during 2005, Antarct. Sci., 26(1), 104–112, https://doi.org/10.1017/S0954102013000382, 2014.

Bailey, M.P. , Hallett, J.: A Comprehensive Habit Diagram for Atmospheric Ice Crystals: Confirmation from the Laboratory, AIRS II, and Other Field Studies, J..Atm..Sci., 61, 2888–2899, https://doi.org/10.1175/2009JAS2883.1, 2009.

Bracci, A., Baldini, L., Roberto, N., Adirosi, E., Montopoli, M., Scarchilli, C., Grigioni, P., Ciardini, V., Levizzani, V.,Porcù, F.:Quantitative Precipitation Estimation over Antarctica Using Different *Ze-SR* Relationships Based on Snowfall Classification Combining Ground Observations. Remote Sens. 2022, 14, 82. https://doi.org/10.3390/rs14010082, 2022.

Bromwich, D. H.: Snowfall in high southern latitudes, Rev. Geophys., 26(1), 149–168, https://doi.org/10.1029/RG026i001p00149, 1988.

Del Guasta, M.: CNN for the classification of ICE-CAMERA images of Antarctic ice particles**,** Zenodo [code], https://doi.org/10.5281/zenodo.6822140, 2022.

Deng,J. Dong,W., Socher R., Li,L-J., Li,K., and Li, F-F.: ImageNet: A large-scale hierarchical image database, IEEE Conference on Computer Vision and Pattern Recognition, 248-255, https://doi.org/10.1109/CVPR.2009.5206848, 2009.

Eidevåg,T., Abrahamsson, P.., Eng M., and Rasmuson A.,Modeling of dry snow adhesion during normal impact with surfaces, Powder Technology, 361, 1081-1092, https://doi.org/10.1016/j.powtec.2019.10.085, 2020

816 Fujita, K., Abe, O.: Stable isotopes in daily precipitation at Dome Fuji, East Antarctica, Geophys. Res. Lett., 33, L18503,
817 https://doi.org/10.1029/2006GL026936, 2006.
818
819 Garrett, T. J., Fallgatter, C., Shkurko, K., Howlett, D.: Fall speed measurement and high-resolution multi-angle photography
820 of hydrometeors in free fall, Atmos. Meas. Tech., 5, 2625–2633, https://doi.org/10.5194/amt-5-2625-2012, 2012
821
822 Genthon, C., Six, D., Gallée, H., Grigioni, P., Pellegrini, A.: Two years of atmospheric boundary layer observations on a 45-
823 m tower at Dome C on the Antarctic plateau, J. Geophys. Res. Atmos., 118, 3218– 3232, https://doi.org/10.1002/jgrd.50128,
824 2016
825
826 Genthon, C., Veron, D. E., Vignon, E., Madeleine, J.-B., Piard, L.: Water vapor in cold and clean atmosphere: a 3-year data
827 set in the boundary layer of Dome C, East Antarctic Plateau, Earth Syst. Sci. Data, 14, 1571–1580,
828 https://doi.org/10.5194/essd-14-1571-2022, 2022.
829
830 Grazioli, J., Tuia, D., Monhart, S., Schneebeli, M., Raupach, T., and Berne, A.: Hydrometeor classification from two-
831 dimensional video disdrometer data, Atmos. Meas. Tech., 7, 2869–2882, https://doi.org/10.5194/amt-7-2869-2014, 2014.
832
833 Grazioli, J., Genthon, C., Boudevillain, B., Duran-Alarcon, C., Del Guasta, M., Madeleine, J.-B. and Berne, A.: Measurements
834 of precipitation in Dumont d'Urville, Adélie Land, East Antarctica, The Cryosphere, 11, 1797–1811,
835 https://doi.org/10.5194/tc-11-1797-2017, 2017.
836
837. Grazioli, J., Madeleine, J.B., Gallée,H., Forbes, R.M, Genthon,C., Krinner ,G., Berne, A. Katabatic Winds Diminish
838 Precipitation Contribution to the Antarctic Ice Mass Balance. *PNAS*, https://doi.org/10.1073/pnas.1707633114, 2017.
839
840 Ham,F.S.:Shape-preserving   solutions   of   the   time-dependent   diffusion   equation, Quart..Appl.Math. **17**,137-145
841 https://doi.org/10.1090/qam/108196, 1959.
842
843 Heymsfield, A. J., Protat, A., Bouniol, D., Austin, R. T., Hogan, R. J., Delanoë, J., Okamoto, H., Sato, K., van Zadelhoff, G.,
844 Donovan, D. P., Wang, Z: Testing IWC Retrieval Methods Using Radar and Ancillary Measurements with In Situ Data, Journal
845 of Applied Meteorology and Climatology, 47(1), 135-163. Retrieved Jun 28, 2022, https://doi.org/10.1175/2007JAMC1606.1,
846 2008.
847
848 Hiley, M. J. , Kulie, M.S., Bennartz R.: Uncertainty Analysis for CloudSat Snowfall Retrievals, Journal of Applied
849 Meteorology and Climatology, 50, 2 ,399-418, 2011.
850
851 Hogan, A. W.: Summer Ice Crystal Precipitation at the South Pole. ,J. of Appl. Meteorol.,14, 2, 246-248,
852 https://doi.org/10.1175/1520-0450(1975)014<0246:SICPAT>2.0.CO;2, 1975.
853
854
855 Huffman, G. J., Adler, R. F., Morrissey, M. M., Bolvin, D. T., Curtis, S., Joyce, R., McGavock, B., Susskind, J.: Global
856 Precipitation at One-Degree Daily Resolution from Multisatellite Observations. Journal of Hydrometeorology 2, 1, 36-50,
     https://doi.org/10.1175/1525, 2001.

857 Hu, MK.: Visual pattern recognition by moment invariants, Information Theory, IRE Transactions, 8, 179-187,
858 https://doi.org/10.1109/TIT.1962.1057692, 1962.

859 Jambon-Puillet, E., Shahidzadeh, N. and Bonn, D.: Singular sublimation of ice and snow crystals. Nature Commun. 9**,** 4191.

860 https://doi.org/10.1038/s41467-018-06689-x, 2018.

861 Kikuchi, K., Hogan A.W.: Properties of Diamond Dust Type Ice Crystals Observed in Summer Season at Amundsen-Scott

862 South Pole Station, Antarctica, J. of the Meteorol. Soc. of Japan. Ser. II, 57, 2, 180-

863 190, https://doi.org/10.2151/jmsj1965.57.2_180, 1979.

864 Kikuchi, K., Kameda, T., Higuchi, K., Yamashita, A.: A global classification of snow crystals, ice crystals, and solid

865 precipitation based on observations from middle latitudes to polar regions, Atmos. Res.,132,460–472,

866 https://doi.org/10.1016/j.atmos.res.2013.06.006, 2013.

867

868 Konishi H., Muramoto K., Shiina T., Endoh T., Kitano K.: Z-R relation for graupels and aggregates observed at Syowa

869 station, Antarctica. Proc. NIPR Symp. Polar Meteorol. Glaciol.,5 ,97-103,1992.

870

871 Lachlan-Cope, T., Ladkin, R., Turner, J., & Davison, P. :Observations of cloud and precipitation particles on the Avery Plateau,

872 Antarctic Peninsula. Antarctic Science, 13(3), 339-348. https://doi.org/10.1017/S0954102001000475,2001

873 Lamb, D.,Hobbs, P. V.: Growth Rates and Habits of Ice Crystals Grown from the Vapor Phase, Journal of Atmospheric

874 Sciences, 28(8), 1506-1509, https://doi.org/10.1175/1520-0469(1971)028<1507:GRAHOI>2.0.CO;2, 1971.

875 Lawson, R. P., Baker, B. A., Zmarzly, P., O'Connor, D., Mo, Q., Gayet, J., Shcherbakov, V. Microphysical and Optical

876 Properties of Atmospheric Ice Crystals at South Pole Station, Journal of Applied Meteorology and Climatology, 45(11),

877 1505-1524. https://doi.org/10.1175/JAM2421.1, 2006.

878 LeCun, Y., Bengio, Y., Hinton, G.: Deep learning. Nature ,521, 436–444, https://doi.org/10.1038/nature14539, 2015.

879

880 Libbrecht ,K.G.: The physics of snow crystals. Rep. Prog. Phys., 68, 855–895, https://doi.org/10.1088/0034-4885/68/4/R03,

881 2005.

882

883 Libbrecht, K.G.: Physical Dynamics of Ice Crystal Growth. Annual Review of Materials Research. 47.

884 https://doi.org/10.1146/annurev-matsci-070616-124135, 2017.

885

886 Libois, Q., Picard, G., Arnaud, L., Morin, S., and Brun, E.: Modeling the impact of snow drift on the decameter-scale

887 variability of snow properties on the Antarctic Plateau, J Geophys Res Atmos, 119, 662–681,

888 https://doi.org/10.1002/2014JD022361, 2014.

889

890 Lindqvist, H., Muinonen, K., Nousiainen, T., Um, J., McFarquhar, G. M., Haapanala, P., Makkonen, R. and Hakkarainen,

891 H. : Ice-cloud particle habit classification using principal components, J. Geophys. Res., 117, D16206,

892 https://doi.org/10.1029/2012JD017573, 2012.

893

894 Liu, G.,Deriving snow cloud characteristics from cloudsat observations,J. Geophys. Res. Atmos., 113 , D00A09,

895 https://doi.org/ 10.1029/2007JD009766, 2008.

896

897 Magono, C., Lee, C. W.: Meteorological classification of natural snow crystals. J. of the Faculty of Sci., Hokkaido
898 University. Series 7, Geophysics, 2(4), 321-335, 1966.
899

900 Nelson, J.: Sublimation of Ice Crystals, Journal of the Atmospheric Sciences, 55(5), 910-919. https://doi.org/10.1175/1520-
901 0469(1998)055<0910:SOIC>2.0.CO;2, 1988.
902

903 Ohtake, T. and Yogi T.: Winter ice crystals at the South Pole. Antarct. J. U.S., 14, 201–203, 1979.
904

905 Palerme, C., Kay, J. E., Genthon, C., L'Ecuyer, T., Wood, N. B., and Claud, C.: How much snow falls on the Antarctic ice
906 sheet?, The Cryosphere, 8, 1577–1587, https://doi.org/10.5194/tc-8-1577-2014, 2014.
907

908 Palerme,C., Claud C., Dufour,A., Genthon,C., Wood N.B., L'Ecuyer,T.: Evaluation of Antarctic snowfall in global
909 meteorological reanalyses, Atmospheric Research, 190, 104-112, https://doi.org/10.1016/j.atmosres.2017.02.015,2017.
910

911 Pratt, W. K.: Digital Image Processing: PIKS Scientific Inside, Fourth Edition, John Wiley & Sons, Inc., Los Altos,
912 California, https://doi.org/10.1002/0470097434, 2006.
913

914 Praz, C., Roulet, Y.-A., and Berne, A.: Solid hydrometeor classification and riming degree estimation from pictures collected
915 with a Multi-Angle Snowflake Camera, Atmos. Meas. Tech., 10, 1335–1357, https://doi.org/10.5194/amt-10-1335-2017,
916 2017.
917

918 Ryzhkin I.A.,Petrenko V.F., Physical Mechanisms Responsible for Ice Adhesion, *J. Phys. Chem. B* 1997, 101, 32, 6267–6270,
919 https://doi.org/10.1021/jp9632145,1977.
920

921 Russ, J.C. and Brent Neal, F.: The Image Processing Handbook 7th Edition, CRC Press, pp 1053,
922 https://doi.org/10.1201/b18983, 2017.
923

924 Santachiara, G., Belosi, F., Prodi, F.: Ice crystal precipitation at Dome C site (East Antarctica), Atmos. Res. 167, 108-117,
925 https://doi.org/10.1016/j.atmosres.2015.08.006, 2016.
926

927 Satow, K.: Observations on the Shapes of Snow Crystals in the Summer Season in Mizuho Plateau, Antarctica, Memoirs of
928 National Institute of Polar Research. Special issue, 29, 103-109, 1983.

929 Schlosser, E., Dittmann, A., Stenni, B., Powers, J. G., Manning, K. W., Masson-Delmotte, V., Valt, M., Cagnati, A.,
930 Grigioni, P., Scarchilli, C.: The influence of the synoptic regime on stable water isotopes in precipitation at Dome C, East
931 Antarctica, The Cryosphere, 11, 2345–2361, https://doi.org/10.5194/tc-11-2345-2017, 2017.

932 Schmidhuber, J.: Deep Learning in Neural Networks: An Overview. Neural Networks, 61, 85-
933 117,https://doi.org/10.1016/j.neunet.2014.09.003, 2014.
934

935 Schneider, U., Finger, P., Meyer-Christoffer, A., Rustemeier, E., Ziese, M., Becker, A.: Evaluating the Hydrological Cycle
936 over Land Using the Newly-Corrected Precipitation Climatology from the Global Precipitation Climatology Centre
937 (GPCC). *Atmosphere* **2017**, *8*, 52. https://doi.org/10.3390/atmos8030052, 2017.

938

939 Shorten, C., Khoshgoftaar, T.M.: A survey on Image Data Augmentation for Deep Learning. *J Big Data* 6, 60,
940 https://doi.org/ 10.1186/s40537-019-0197-0, 2019.

941 Shimizu, H., ''Long prism'' crystals observed in the precipitation in Antarctica. J. Meteor. Soc. Japan, **41,** 305–307.
942 https://doi.org/10.2151/jmsj1923.41.5_305, 1963.

943

944 Smiley, V. N., Whitcomb, B. M., Morley, B. M., & Warburton, J. A.: Lidar Determinations of Atmospheric Ice Crystal
945 Layers at South Pole during Clear-Sky Precipitation. Journal of Applied Meteorology, 19,9, 1074–1090, 1980.

946

947 Souverijns,N., Gossart,A., Lhermitte, S., Gorodetskaya I.V., Kneifel,S., Maahn,M., Bliven,F.L., van Lipzig,.P.M.:Estimating
948 radar reflectivity - Snowfall rate relationships and their uncertainties over Antarctica by combining disdrometer and radar
949 observations, Atmospheric Research,196, 211-223, https://doi.org/10.1016/j.atmosres.2017.06.001.2017,2017.

950 Szegedy,C ., Liu,W., Jia,Y., Sermanet P., Reed S.,, Anguelov D., Erhan D., Vanhoucke V. and Rabinovich A.: "Going
951 deeper with convolutions," 2015 IEEE Conference on Computer Vision and Pattern Recognition (CVPR), 1-9,
952 https://doi.org/10.1109/CVPR.2015.7298594, 2015.

953 Tremblin, P., Minier,V., Schneider,N., Durand, G. Al. , Ashley, M. C. B. , Lawrence, J. S. , Luong-Van, D. M. , Storey,
954 J. W. V. , Durand, G. An. , Reinert, Y., Veyssiere, C., Walter, C., Ade, P. , Calisse, P. G., Challita, Z. , Fossat, E. ,
955 Sabbatini, L., Pellegrini, A., Ricaud, P., Urban, J. : Site testing for submillimetre astronomy at Dome C, Antarctica, A&A
956 535 A112, https://doi.org/10.1051/0004-6361/201117345, 2011.

957 Vignon, E., Genthon, C., Barral, H., Amory, C., Picard, G., Gallée, H., Casasanta, G., and Argentini, S.: Momentum and heat
958 flux parametrization at Dome C, Antarctica: a sensitivity study, Boundary-Layer Meteorol, 162, 341–367,
959 https://doi.org/10.1007/s10546-016-0192-3, 2016.

960 Vignon, E., Genthon, C., Barral, H.,Amory, C., Picard, G., Gallée, H., Casasanta, G., Argentini, S.: Momentum- and Heat-
961 Flux Parametrization at Dome C, Antarctica: A Sensitivity Study. Boundary-Layer Meteorology. https://doi.org/
962 10.1007/s10546-016-0192-3, 2017.

963 Walden, V. P., Warren, S. G., Tuttle, E. (2003). Atmospheric Ice Crystals over the Antarctic Plateau in Winter, Journal of
964 Applied Meteorology, 42(10), 1391-1405,https://doi.org/10.1175/1520-0450(2003)042<1391:AICOTA>2.0.CO;2, 2003.

965 Walton,W.: Feret's Statistical Diameter as a Measure of Particle Size, Nature, **162,** 329–330,
966 https://doi.org/10.1038/162329b0, 1948.

967

968 Xiao, H., Zhang, F., He, Q., Liu, P., Yan,F., Miao, L. and Yang, Z. : Classification of ice crystal habits observed from airborne
969 Cloud ParticleImager by deep transfer learning., Earthand Space Science, 1877–1886, https://doi.org/10.1029/2019EA000636,
970 2019.

971

972 Wood, N., L'Ecuyer, T., Heymsfield, A. , Stephens, G. : Microphysical Constraints on Millimeter-Wavelength Scattering
973 Properties of Snow Particles. Journal of Applied Meteorology and Climatology. 54. 909-931. https://doi.org/10.1175/JAMC-
974 D-14-0137.1, 2015.

975

976 Zheleznyak, A.G. , Sidorov, V.G.: Flatbed scanner as an instrument for physical studies,St. Petersburg Polytechnical

977 University Journal: Physics and Mathematics, 1, Issue 2, 134-141,https://doi.org//10.1016/j.spjpm.2015.04.001. 2015.

978